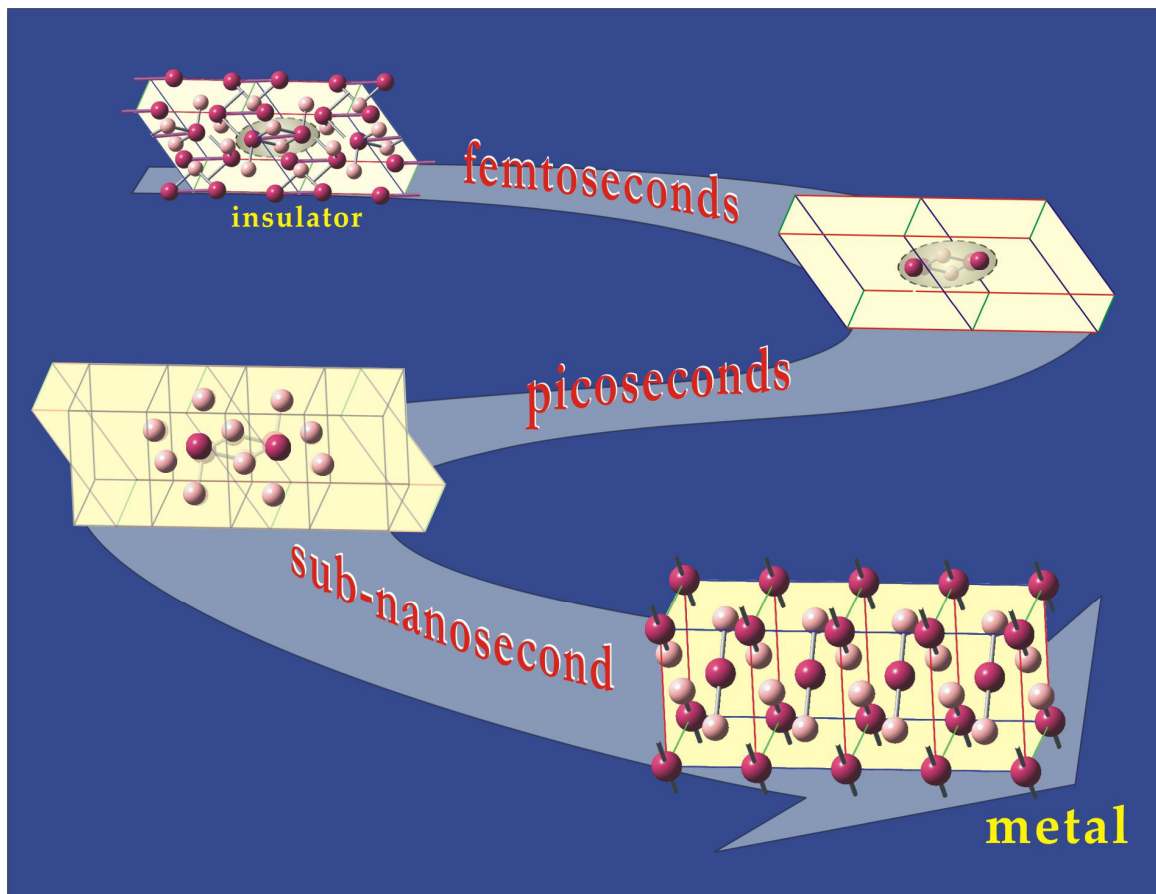


Part II

Highly Correlated Materials

Chapter 6

Four-dimensional Visualization of Transitional Structures in Phase Transformations[†]



[†]Full account for a previous report by P. Baum, D.-S. Yang, A. H. Zewail *Science* **318**, 788 (2007).

Introduction

A first-order phase transition, which depicts the transformation between two distinct phases of a material at a well-defined temperature, is conventionally achieved through a change in a field variable such as pressure, temperature, magnetic or electric field. The most common examples are those transformations between the solid, liquid and gas states of matter; for such phase transitions, the general macroscopic, thermodynamic description has been established for many decades. However, since a phase transition is not achieved instantaneously, a microscopic understanding of the phenomenon, which demands the knowledge of the transformation mechanisms in advance, is critical to the dynamic description and the kinetics of the transition processes in time. In cases of melting (freezing), vaporization (condensation) and sublimation (deposition), interactions between atoms or molecules, and nucleation and the growth of nuclei accompanying the absorption (release) of thermal energy, are central in the microscopic description (1).

As a phase transformation involves collective phenomena, unraveling the relevant microscopic processes at work can be a daunting task. The metal–insulator transition (2) is such a transformation with a quantum nature, signifying the abrupt state change between the existence of a massive number of interacting, itinerant electrons and their localization into an ordered, bounded conformation (3). One of the best known examples is vanadium dioxide (VO_2), which has been a subject of intensive study for nearly half a century (4-13) since the discovery of its first-order metal–insulator transition at a temperature of ~ 340 K by Morin (14). The further complication in its study is the accompanied structural transformation at a very similar, if not exactly the same, temperature between the low-temperature monoclinic (M_1) and high-temperature tetragonal (rutile) crystal structures (15, 16). As a result, for the strongly correlated

material VO₂, the issue of whether the phase transition at $T = 340$ K is essentially originated from the electron correlation effect [the Mott–Hubbard picture (7, 17)] or dominated by the structural vanadium–vanadium (V–V) dimerization/separation [the Peierls picture (5, 18)] has long been under debate until even today (19, 20). The question of whether or not the temperature of the metal–insulator transition and that of the structural transformation are the same has also been raised and argued (21).

To resolve these puzzles satisfactorily, it is more important to look into the dynamics involved in the phase transformation(s), besides understanding the properties of the individual phases. In this regard, the difference in the characteristic time scales for charge carriers and nuclear motions (lattice vibrations) may provide hints to a deeper understanding. It is known that the transformation from the insulating monoclinic phase of VO₂ to the metallic tetragonal phase can also be initiated via photoexcitation of the valence electrons (22-27); through the photoreflectivity and phototransmission experiments that are sensitive to the dynamics of the excited carriers, their internal equilibrium is reached in an ultrashort time of ~ 80 fs (28). In contrast, nuclear motions generally occur on a longer time scale, from hundreds of femtoseconds for interatomic vibrations (29) to up to tens of picoseconds for lattice expansion over many unit cells (Chs. 4, 5 and 7). Thus, unifying the concomitance of the electronic metal–insulator transition and the structural lattice transformation (from thermodynamic studies) with this temporal disjunction between the electronic and structural equilibriums (in the dynamics) may be the key to settling down the aforementioned debates over many decades.

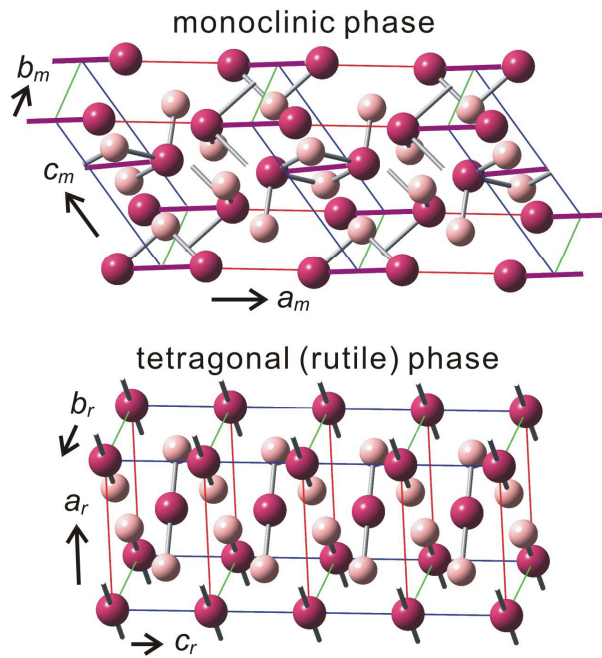
In fact, we want to point out that the description of only two states (the insulating monoclinic and metallic tetragonal phases) involved during the phase transition process of VO₂ is incompatible with the dynamical behavior observed using time-resolved

techniques. The ultrashort time of 80 fs, in which the initial insulating VO₂ appears to already reach a metallic state (28), is too short for all the nuclei to arrive at their final positions in the tetragonal structure. With a sound speed of ~4000 m/s in this material (30), a distance of ~3 Å would be the upper limit for any nuclear motion in such an ultrashort time; however, the size change of a sub-micrometer crystallite, e.g., the accumulated *b*-axis expansion over 1000 unit cells, is about an order of magnitude larger than the 3-Å limit, let alone the accumulated nuclear movements due to the angular change between the principal axes *a* and *c* (31). Therefore, there must be some transitional state(s) during this solid-solid phase transformation, and the identification and even visualization is of the utmost importance.

This concept of the energy landscape and transition and intermediate states has been widely used for reactions and transformations in chemistry and biology; in condensed matter, such use has recently been theoretically addressed for solid-solid transitions involving two thermodynamically stable configurations (32, 33). Experimentally, for direct probing of the transitional state(s) during phase transformations, the radiation or particle used must have both a wavelength on the scale of atomic distances and an appropriate temporal resolution, as demonstrated in the studies of melting and lattice dynamics by ultrafast X-ray absorption (34) and diffraction (35-38), and electron diffraction (39-41). In our laboratory, ultrafast electron microscopy and diffraction (42) have been the methods of choice for direct observation of the structural dynamics during molecular and phase transitions (43-45).

In this chapter, I provide a full account of the structural evolution during the solid–solid phase transformation of VO₂ from the initial monoclinic conformation to the final tetragonal one, using time-resolved electron diffraction with atomic-scale spatial

(a) Real space



(b) Reciprocal space

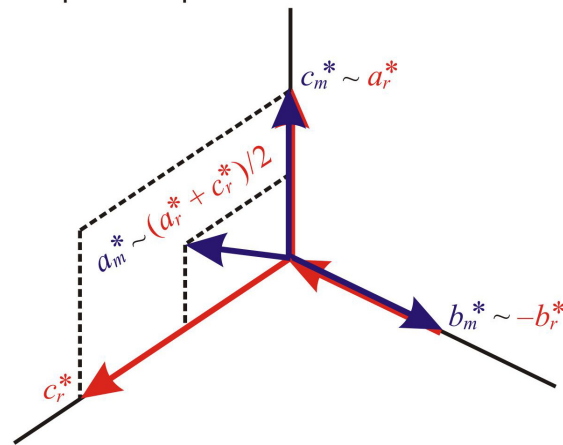


Fig. 1. Real-space crystal structures of VO_2 and the corresponding basis vectors in reciprocal space. (a) Crystal structure of the monoclinic, low-temperature phase (upper panel) and the tetragonal (rutile), high-temperature phase (lower panel). Vanadium atoms are depicted in red and oxygen atoms in pink. The major structural difference is the V–V dimers (indicated by violet lines) in the monoclinic phase and their breakage in the tetragonal phase. Note that the axis definitions change. (b) The relationship between the reciprocal basis vectors for the two phases.

and temporal resolution (46). Experiments were performed mainly on VO₂ single crystals, and on a thin-film sample to gather more data for the fluence dependence results. In order to map pathways of nuclear motion, all observed Bragg diffractions of different planes and zone axes were examined on the femtosecond to nanosecond time scale. The match between the observed temporal changes and the calculated structure factor for various indices makes possible the separation of different nuclear motions—the femtosecond primary V–V bond dilation, the displacements of atoms in picoseconds, and the sound-wave shear motion on ~100 ps. Moreover, we found that a minimum fluence of photoexcitation is required to activate the structural transformation at short and long times, and this threshold behavior has a clear dependence on the ambient temperature. The fairly good correspondence between the excitation threshold observed in the photoinduced phase transformation and the thermal energy required by the phase transition thermodynamically at different temperatures convincingly indicates a common transformation mechanism for both scenarios. Thus, with the examination of the thermodynamic studies in recent years (12, 13, 19), the present study of structural dynamics offers a unified delineation for this highly correlated material of VO₂.

Experimental Section and Sample Characterization

A. VO₂ Single Crystals

The two thermodynamically stable crystal structures of VO₂ are depicted in Fig. 1a: the vanadium atoms arrange into pairs in the initial monoclinic M_1 phase, whereas all V–V distances are equal in the final tetragonal phase. The crystal axes are assigned differently due to the symmetry change, and the a axis of the M_1 phase is conventionally matched with the c axis of the tetragonal phase. Therefore, in real space,

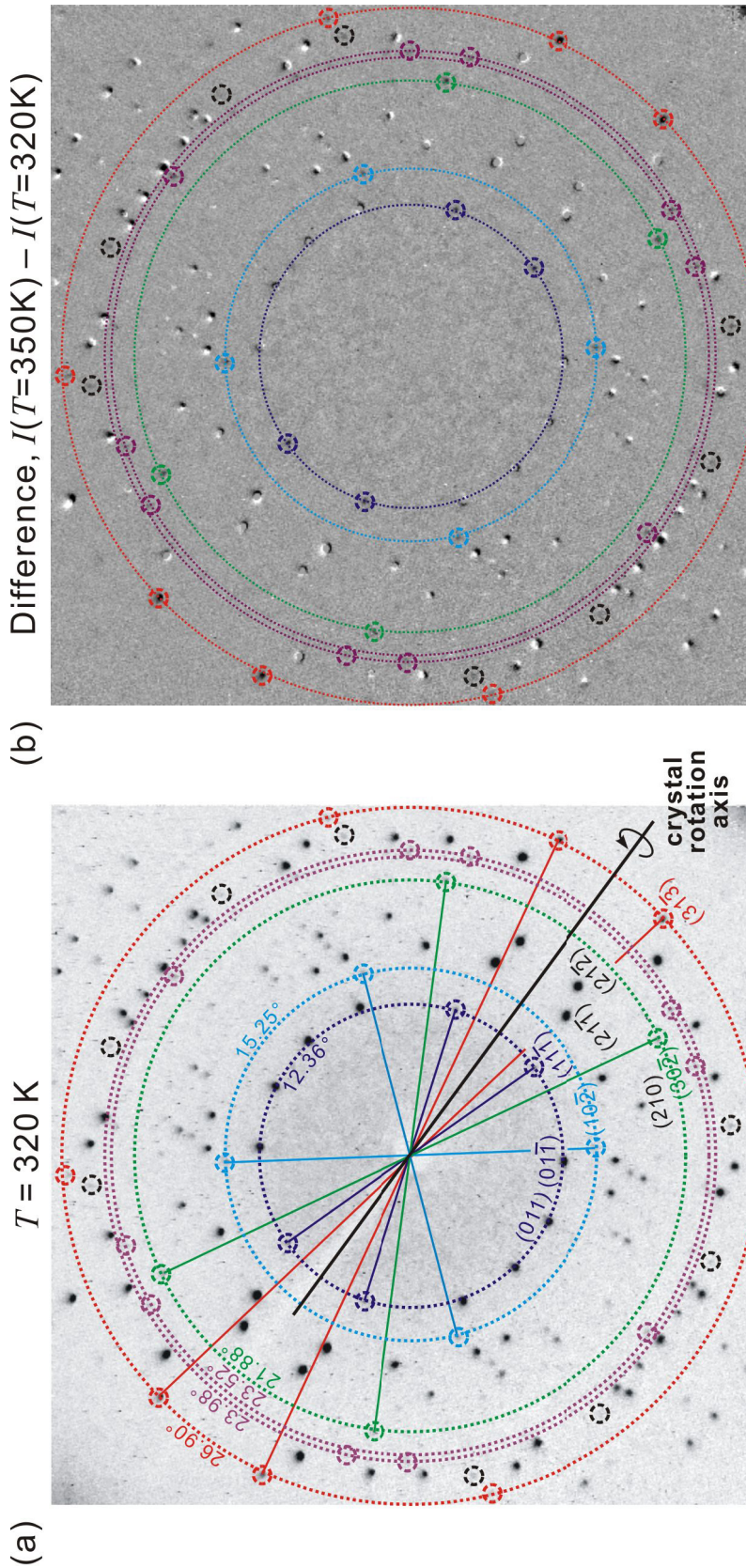
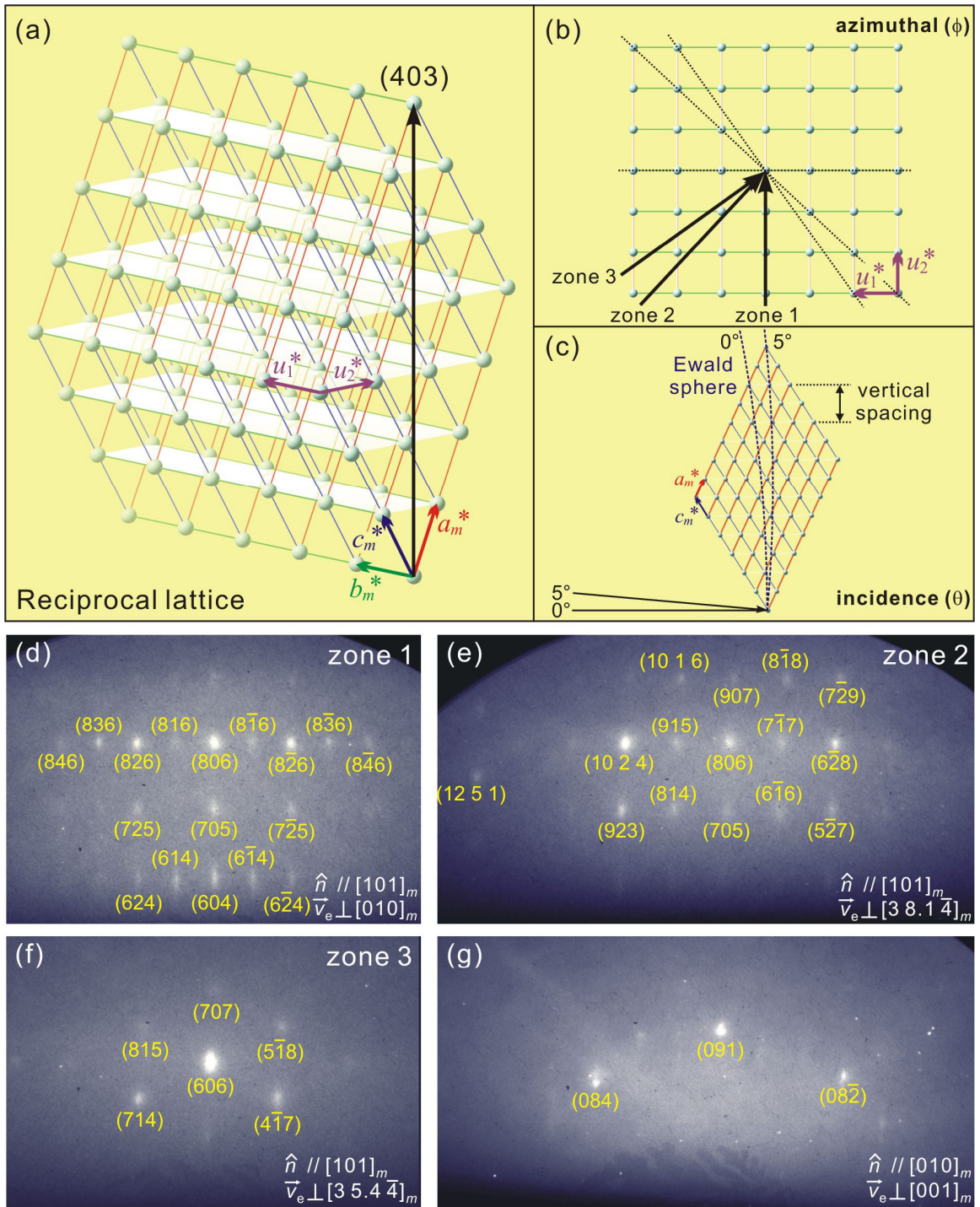


Fig. 2. (a) X-ray diffraction pattern of the low-temperature M_1 phase, obtained by the rotating crystal method. The solid lines connect symmetry-related spots, and indices of a few spots are given. Small dashed circles (on concentric dotted circles with the corresponding scattering angles) indicate those diffractions with an odd h index. (b) Difference of the x-ray patterns from the two phases. Total loss of intensity (appearing as a pure dark spot) is seen for those diffractions encircled by the small dashed circles; other spots show both white and dark parts along the angular direction, signifying a small rotation of the crystal axes between the two phases.

$a_m \sim 2c_r$, $b_m \sim -b_r$ and $c_m \sim a_r - c_r$, where the subscripts m and r refer to the M_1 and rutile (i.e., tetragonal) structures, respectively. The basis vectors in reciprocal space can be deduced, as shown in Fig. 1b. It is clear that any reciprocal lattice point $(hkl)_m$ for the M_1 phase has one-to-one correspondence with one for the tetragonal phase, i.e. $(\frac{h}{2}+l, -k, \frac{h}{2})_r$, except for those with an odd h . Thus, the Bragg diffractions from the M_1 phase with an odd h index become forbidden after the structural transformation into the tetragonal phase; all other diffractions are allowed, with certain changes in their intensities and slight shifts in their positions due to the small modification in the unit-cell parameters (31).

In order to minimize or eliminate the effects from the sample inhomogeneity and morphology, stoichiometric deviation, embedded defects, domain sizes, etc., we used single crystals for the current study of structural dynamics in VO₂. Three single crystals of VO₂ with a phase-transition temperature near 340 K have been grown by the vapor transport method (47), and were from the same source as those samples in Refs. 12 and 13. Static X-ray diffraction (by a Bruker SMART 1000 CCD diffractometer with graphite monochromated Mo K_α radiation, $\lambda = 0.71073 \text{ \AA}$) was performed for the confirmation of the crystal structures below and above 340 K; the long-range order of the samples was evident from the well-defined diffraction spots shown in Fig. 2. Dotted circles are drawn to indicate those diffractions with an odd h index in the M_1 phase, which are encircled in small dashed circles. Above 340 K, they become forbidden due to the change in the structural symmetry and therefore disappear, showing complete loss of diffraction intensity (appearing as dark spots at the same positions in the difference image, Fig. 2b). All other spots show both bright and dark parts in the difference image, indicating the slight changes in the Bragg spot positions upon the structural transformation. It is noted that most of the shifts contain a clear angular component, which signifies the small



(See next page for the figure caption.)

Fig. 3. Ewald construction in reciprocal space and diffraction patterns observed by UEC. (a) The corresponding reciprocal lattice for the crystal that was mechanically cut and polished; the exposed surface is the $(403)_m$ plane, whose surface normal direction is along the black arrow. Purple arrows are the basis vectors for the plane. (b) Top view of the two-dimensional reciprocal lattice for the $(403)_m$ plane and the three zone axes (indicated by the dashed lines and black arrows) accessed through the azimuthal rotation. (c) Side view of the Ewald construction (along \vec{b}_m^*) for satisfaction of the diffraction condition. The vertical separation between the observed Bragg spots is related to the reciprocal vector, $\vec{a}_m^* + \vec{c}_m^*$, at the electron incidence angle of 5° . (d–g) Typical diffraction patterns observed from different crystal surfaces and different zone axes; \hat{n} is the surface normal direction and \vec{v}_e is the electron propagation direction (zone axis). All Bragg spots can be identified as the monoclinic structure (yellow indices).

angular movements of atoms, or equivalently, a slight rotation of the crystal axes, in accord with a previous study (31). Such angular modification causes a shear motion in VO₂ during the phase transition, and it will be shown later that this shear motion plays an important role in the dynamics of the photoinduced phase transition at longer times.

The naturally grown crystal surfaces typically have an area of $\sim 2 \times 2 \text{ mm}^2$. Sometimes even without the process of cleaving or major cleaning, a pattern of well-indexed Bragg spots can be obtained by our facility of reflection electron diffraction. When necessary, the crystal surfaces were polished mechanically and gently wiped clean with acetone. The resulting diffraction patterns become transmission-like due to the electrons probing the sub-micrometer-sized islands of VO₂; however, all spots can be correctly indexed, which shows that VO₂ is hard enough and mechanical polishing of its surfaces is feasible. We observed, by monitoring the intensities of Bragg spots from the top surface of a crystal, a complete phase transformation within 3 K and also the hysteresis phenomenon with a width of 5.6 K, at a rate of heating or cooling of $\sim 0.6 \text{ K/min}$ from the bottom of the crystal. Therefore, the numbers reported here for the temperature range and hysteresis width are the upper limits, and the actual values are believed to be smaller (see the inset of Fig. 2 in Ref. 13).

To gather complete crystallographic data for the photoinduced structural dynamics in all three dimensions, one of the crystals was mechanically cut and polished to expose a surface that was not naturally grown and had a nonzero h index. Guided by the information from x-ray diffraction, we obtained the $(403)_m$ plane, whose corresponding two-dimensional lattice in reciprocal space is formed by the orthogonal basis vectors of $u_1^* = b_m^*$ and $u_2^* = a_m^* - c_m^*$ (Fig. 3a). Different zone axes of such a crystal surface can be accessed through the azimuthal rotation (ϕ); three such directions

are indicated in Fig. 3b and the corresponding static diffraction patterns, obtained at an incidence angle of $\sim 5^\circ$ at room temperature, are presented in Fig. 3, panels d to f. The small incidence angle of electrons is required for the proper interception of the Ewald sphere with the reciprocal lattice points, as shown in Fig. 3c. For comparison, a diffraction pattern from the unpolished $(010)_m$ surface of another crystal at a similar incidence angle is given in Fig. 3g.

B. VO₂ Thin Films

It is known that VO₂ crystals are prone to fracture after several cycles of the phase transition thermally because of the mechanical tensions caused by the volume change. We also found that they cannot remain intact under the optical excitation above a certain threshold. Hence, for the temperature- and fluence-dependent experiments, we also used thin-film samples to obtain more data points. However, more caution is needed for the study of dynamics on VO₂ thin films. Many issues, such as wrong stoichiometry, the existence of mixed phases, sample inhomogeneity and morphology, small domain sizes and poor connectivity, embedded impurities, additional strain or binding from the underlying substrate, etc., may substantially alter the structural dynamics and consequently lead to different conclusions from those made in the studies of single crystals. Therefore, a close comparison of the thin-film dynamics with the existing data from single crystals is necessary before it is included for further discussions.

Crystalline VO₂ thin films have been successfully fabricated on single-crystal sapphire (Al₂O₃) substrates by using the pulsed laser deposition (PLD) method (48-51). With a proper choice of the partial pressure of oxygen and the substrate temperature, the deposited films can be highly oriented and single-phased with the correct stoichiometry and no contamination from the substrate (50). Our thin films were prepared with the use

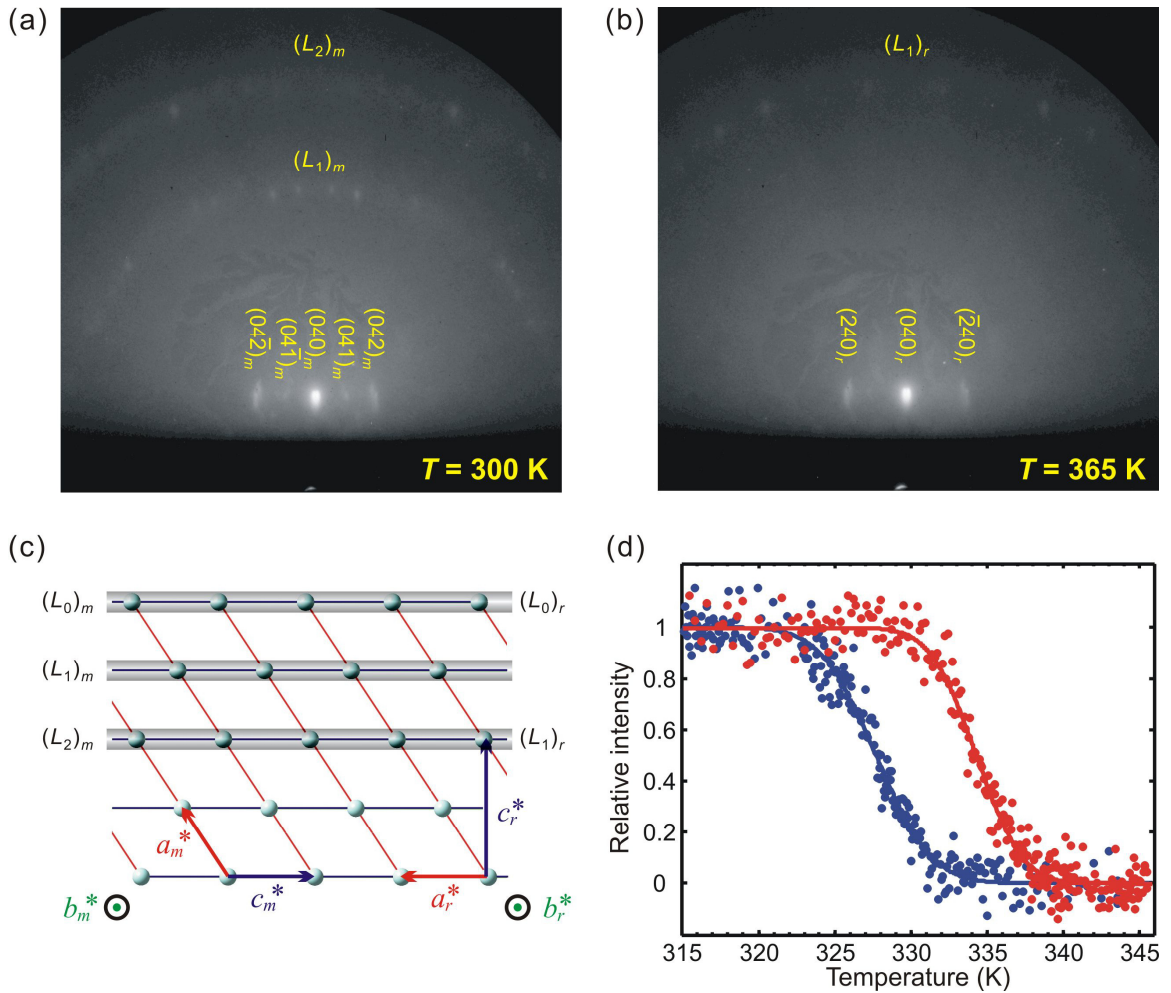


Fig. 4. (a) Reflection diffraction pattern of a VO_2 thin film on $\text{Al}_2\text{O}_3(10\bar{1}0)$, in the low-temperature M_1 phase. Bragg spots from the zeroth-order Laue zone, $(L_0)_m$, are indexed and the first- and second-order Laue zones [$(L_1)_m$ and $(L_2)_m$, respectively] are indicated. (b) Diffraction pattern of the high-temperature phase. While the Bragg spots from the zeroth-order zone remain clear, only the first-order zone, $(L_1)_r$, can be observed. (c) Relationship between the reciprocal lattices for the two phases. In the high-temperature phase, $(L_1)_m$ is forbidden and therefore $(L_2)_m$ becomes $(L_1)_r$. (d) Diffraction intensity of the four $(L_1)_m$ spots in the center as a function of temperature. The red dots and curve are obtained from the heating procedure and the blue from the cooling procedure.

of a KrF excimer laser [COMPex Pro 102(KrF), Coherent], which has an output of ~ 300 mJ per 20-ns pulse at a wavelength of 248 nm. Before deposition, the base pressure in the chamber was on the order of 10^{-6} Torr, and a constant flow of the oxygen (10%) and argon (90%) mixture was then introduced, resulting in a total pressure of 28 mTorr. Light pulses at a repetition rate of 20 Hz were focused onto an area of $\sim 11 \times 1.0$ mm² on a rotating target of pure vanadium metal (99.9%, ESPI Metals); vanadium atoms were ablated to react with oxygen to form oxide films. The rotating sapphire wafers (EPI-polished, MTI) were held at a temperature of 500°C during the film growth, and the typical target-substrate distance was 9 cm. The thickness of the VO₂ films was ~ 140 nm (measured by a contact profilometer) after 10^5 laser shots. To enhance the sample homogeneity, domain size and connectivity, the deposited films were annealed for 42 hours in a pure oxygen atmosphere at 10 mTorr.

The insulator–metal phase transition of the thin films was observed by infrared transmission at 2000 nm (0.62 eV) as a function of temperature. The closing of the band gap of ~ 0.6 eV (4, 13) at high temperature leads to a 30–45% decrease in transmittance and a typical width for the hysteresis phenomenon is ~ 6 K. Among the samples prepared on the Al₂O₃ wafers with different surface planes, we found that VO₂/Al₂O₃(10 $\bar{1}$ 0) was able to produce a nice reflection pattern from electron diffraction, whereas VO₂/Al₂O₃(0001) and VO₂/Al₂O₃(1 $\bar{1}$ 02) readily gave transmission-like patterns. All VO₂ films were highly oriented. In Fig. 4, panels a and b, we present the diffraction patterns from VO₂/Al₂O₃(10 $\bar{1}$ 0) recorded at an incidence angle of 1.75° at two temperatures ($T = 300$ and 365 K, respectively). From the Bragg spots and the noticeable diffractions from the first- and second-order Laue zones, we confirm that the (010) plane of VO₂ is parallel and registers to the wafer plane (10 $\bar{1}$ 0). The structural transformation

can be clearly seen: given the direction of electron probing as in Fig. 4, the first Laue circle, which originates from the reciprocal rods with the index of $h = 1$, disappears as the sample is heated above the transition temperature (Fig. 4c). By gauging the total intensity of the four spots on the middle part of the first Laue circle in Fig. 4a, we observed the phase transformation near 334 K and a hysteresis width of ~ 6 K (Fig. 4d). These values are satisfactorily consistent with those retrieved from the infrared transmission data.

C. Time-resolved Electron Diffraction

We used near-infrared pulses of 800 nm (1.55 eV) to initiate the phase transformation, whose structural dynamics was followed by diffracting the electron packets after a variable delay time. The maximum optical fluence applied was 25 mJ/cm^2 , and a fraction of it was enough to drive the phase transition with a single pulse. The pulse tilting excitation scheme was invoked to resolve the group-velocity mismatch between electrons and light (46). At the small angle of incidence, the electron-probed area on the crystal surface is ~ 2 mm (the sample size) by 0.2 mm (the electron-beam diameter), giving a temporal mismatch as large as 20 ps between the optical excitation and the electron pulses in the original nontilted excitation scheme. By tilting the optical pulse, their temporal synchrony can be achieved on the entire probed crystal surface, reaching a femtosecond temporal resolution convoluted by any residual spread and the involved duration of optical (120 fs) and electron pulses.

Within the experimental repetition period of 1 ms, we observed a full recovery to the initial M_1 phase in all VO_2 samples, which was confirmed by observing no change between the diffraction patterns recorded with the optical excitation at negative delay time (an effective 1-ms delay) and those recorded without the excitation. Thus, the contributions from static heating can be excluded, and the observed diffraction changes

reveal the nonequilibrium dynamics following the femtosecond excitation. From the VO₂ single crystals, we observed tens of well-indexed Bragg spots from the three-dimensional reciprocal space (Fig. 3, panels d to g), and 30 of them were intense enough for time-resolved investigations. They were acquired at short (femtosecond to picosecond) and long (sub-nanosecond to 1.3 ns) times at room temperature. For the detection of the femtosecond dynamics, we used a time step of 250 fs and reduced the number of electrons per pulse to as low as ~500, significantly below the space-charge limit (42). In such a low flux, the electron pulse width has been measured (322 ± 128 fs) *in situ* at a streaking speed of 140 ± 2 fs/pixel (52). After the different stages of the structural transformation of VO₂ were identified, diffraction patterns were recorded with different excitation fluences at two specific delay times, $t = 30$ ps and 1.3 ns. The fluence was adjusted by rotating a polarizer against another fixed one to keep the same polarization. We also performed the same experiment and fluence-dependent study for the structural dynamics at $T \sim 110$ K. From the thin-film sample of VO₂/Al₂O₃(10 $\bar{1}$ 0), the temporal changes of the (040) Bragg spot at room temperature and at ~ 100 K were recorded. They can be well compared with the data obtained from the single crystals, thus provide consistent dynamical information. Fluence-dependent experiments were then carried out at various temperatures.

We also checked for possible effects of surface potential change or charge trapping on the diffraction during the transition from the insulator to metal phase; no such effects were found, as evidenced from our observation of a steady position and intensity of the direct, nondiffracted electron beam for scans at all delay times. At 5° incidence, the electrons diffract from a material thickness of about 10 nm; we do not observe rods in the diffraction patterns, but instead well-defined Bragg spots, suggesting that at least ten

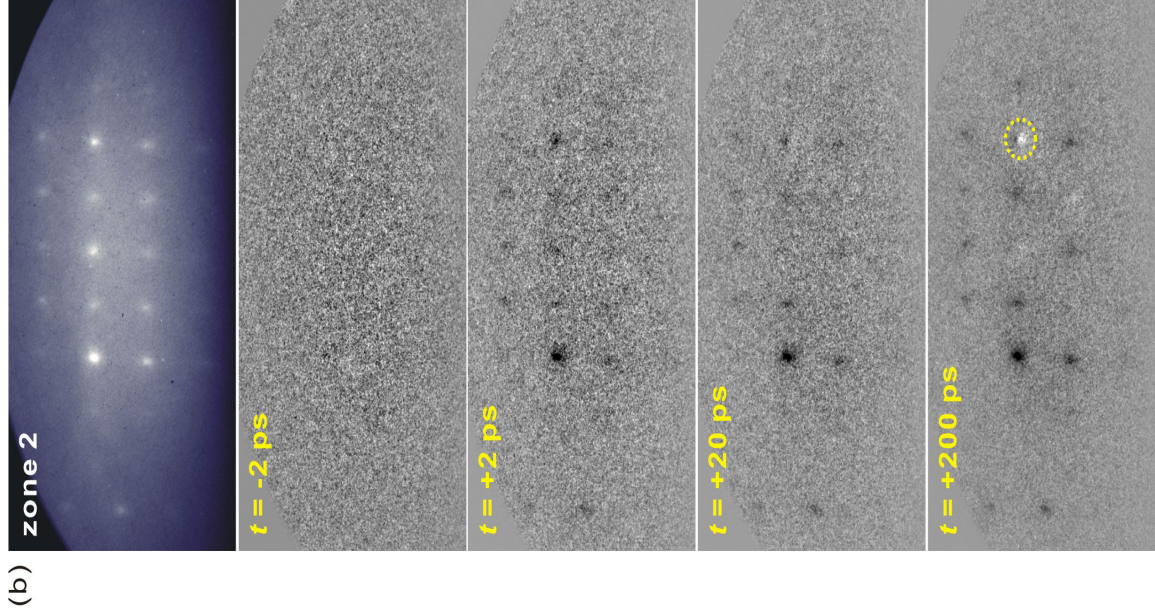
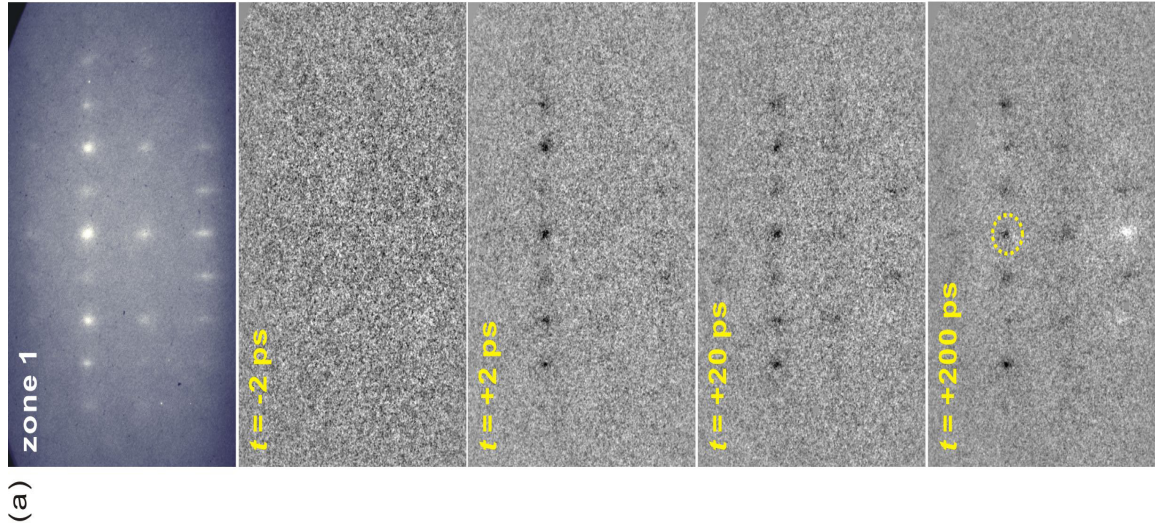


Fig. 5. Diffraction patterns at two zone axes and their time-dependent changes (referenced to the negative time frames), following the femtosecond optical excitation. Before time zero (e.g., $t = -2 \text{ ps}$), no appreciable diffraction difference is observed. At positive times, dark spots signify intensity depletion and white spots signify intensity enhancement; the observation of both dark and white parts for the circled spots at $t = 200 \text{ ps}$ signifies a small position shift of the Bragg diffractions at a later time.

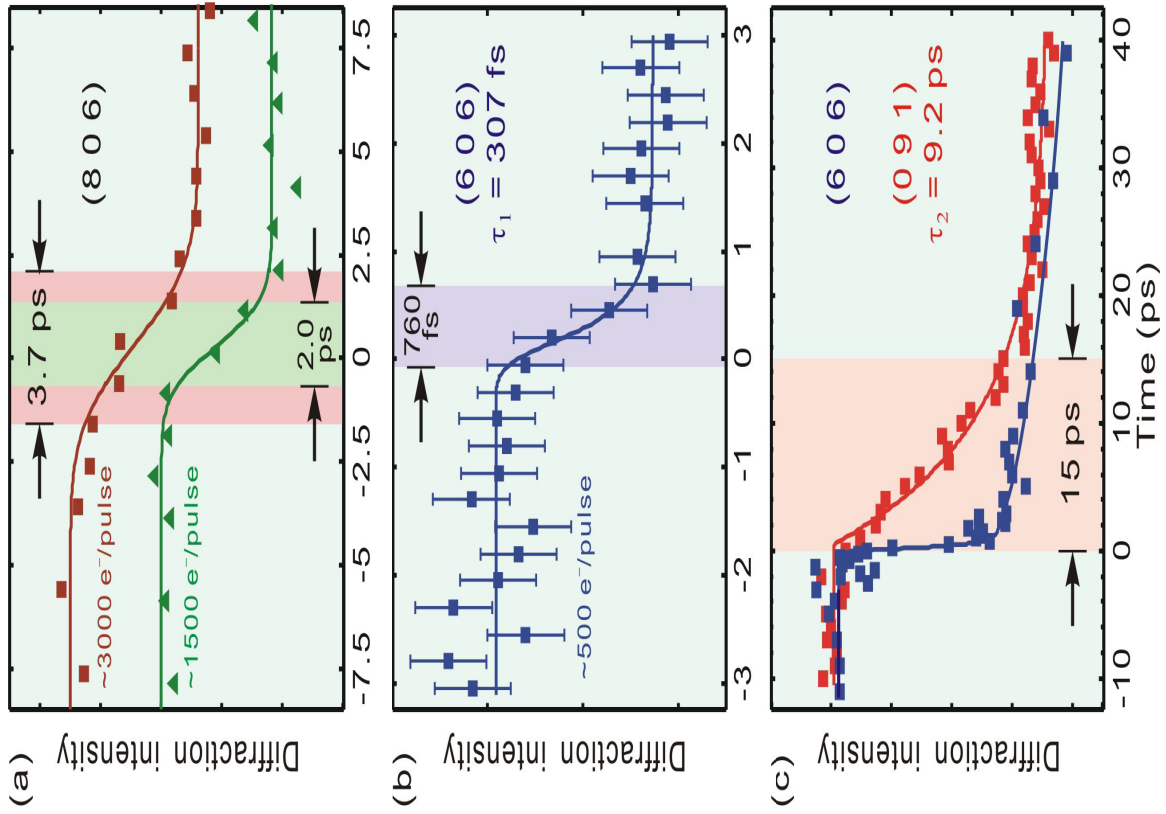


Fig. 6. Ultrafast dynamics of the structural phase transition of VO₂. (a) Intensity change of the (806) Bragg spot with time. The observation was made at a larger number of electrons per pulse. The colored regions indicate the temporal range over which the intensity decrease occurs. The results signify that the ultrafast change is faster than the temporal resolution. (b) Intensity change of the (606) Bragg spot with time. The decay shows an apparent time constant (τ_1) of 307 fs on the total time range of ± 3 ps. (c) Intensity changes of the (606) (blue) and (091) (red) spots with time. A femtosecond decay similar to the blue trace was measured for other spots with a nonzero h index; a decay with a time constant (τ_2) of 9.2 ps, similar to the red trace, is measured for spots with $h = 0$ on the total time range of 40 ps. The temporal range values over which the decay is pronounced are 760 fs in (b) and 15 ps in (c). This difference indicates a stepwise mechanism for atomic motions

interatomic layers in the surface-normal direction are contributing to the interferences. We note that a rough estimate of the mean free path of a 30-keV electron gives a penetration depth (~ 5 nm) that is about 20 times the interplanar separation. By these examinations, we confirm the observed diffraction changes to be from the photoexcited bulk VO₂.

Results and Analysis

The patterns of diffraction change at four selected delay times, which are referenced to a negative time frame, are shown in Fig. 5 for two zone axes at an excitation fluence above 10 mJ/cm². Right before the zero of time, no appreciable difference can be seen, which assures the stability of the data acquisition without a long-term drift. After the zero of time, in only 2 ps, a significant decrease in intensity with no distinct spot movement is observed for some Bragg diffractions; the intensity drop is maintained at a similar level for a period of ~ 20 ps. Further diffraction changes, such as more intensity decrease or reversed increase, and spot position shift, continue to develop within 200 ps, and the resulting diffraction patterns remain steady for the following 1 ns, which reaches the end of our time range. These different periods signify the time scales involved in the photoinduced structural transformation of VO₂. Hence, to quantify the diffraction differences and characteristic times, we fit the horizontal and vertical profiles of the Bragg spots and retrieve the information of spot intensities, positions and widths as a function of time.

The initial intensity decrease at short times is plotted for three different Bragg spots in Fig. 6. Two types of behaviors are seen: an ultrafast decay that seems to be limited by the electron pulse width and a decay that lacks such fast dynamics but

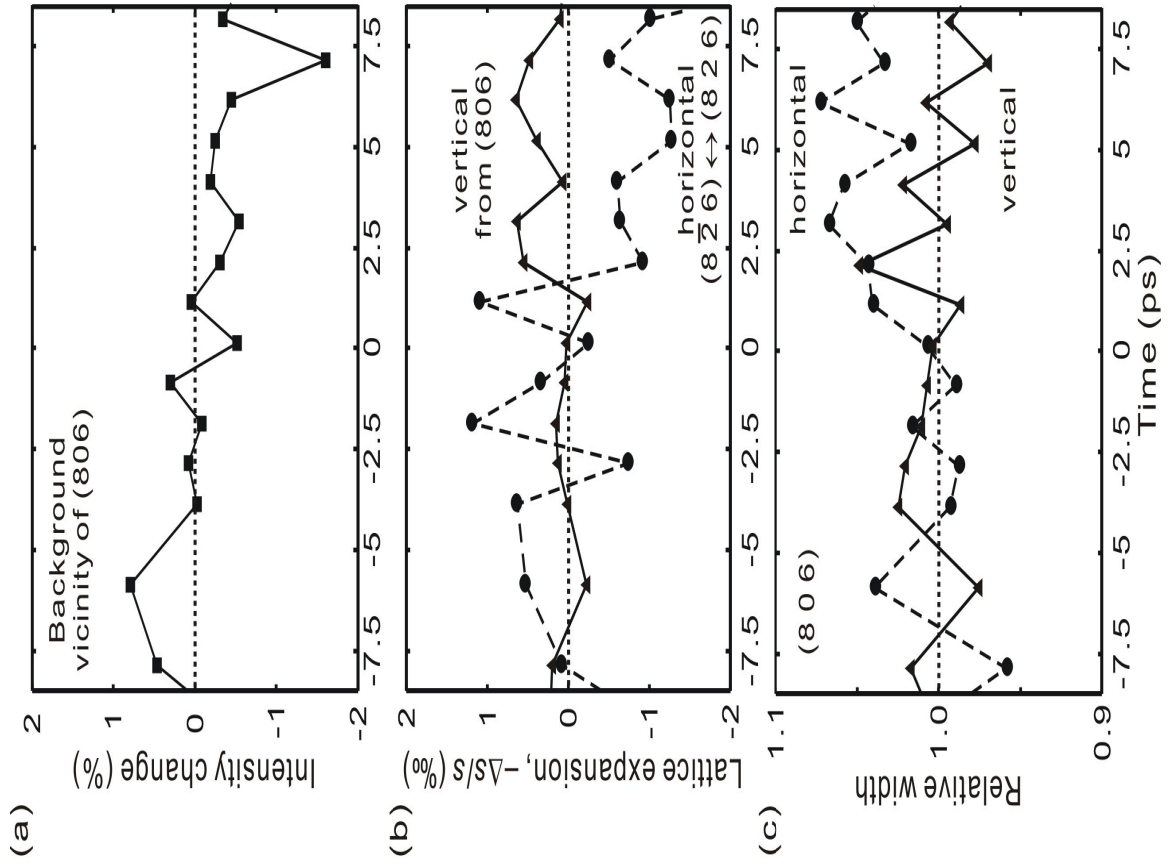


Fig. 7. Other diffraction changes at early delay times. (a) The scattering intensity in the vicinity of the (806) Bragg spot essentially remains at the same level while the diffraction exhibits clear femtosecond intensity decrease. (b) Vertical expansion derived from the position change of the (806) spot and horizontal expansion from the spacing change between the $(8\bar{2}6)$ and (826) spots with time. The Bragg spots keep their original positions at early times, signifying no major unit cell change on this time scale. Note the small scale for the vertical axis. (c) Vertical and horizontal width change of the (806) spot with time. The widths are essentially constant in this time range and their temporal behavior is quite different from those shown in Chs. 4 and 5.

proceeds within a longer period of ~ 15 ps. By lowering the number of electrons per pulse, the full range for the ultrafast intensity decrease can be reduced from 3.7 ps in Fig. 6a to 760 fs in Fig. 6b. Using the cross correlation between the optical pulse width of 120 fs and the electron pulse width of 322 fs at ~ 500 electrons per pulse, we deduce a time constant (τ_1) of 307 fs as an upper bound since the unknown residual spread from the setup for the pulse tilting scheme, broadening of the laser pulse in the optical path, and relative large uncertainty in the electron pulse width are not taken into consideration. This femtosecond behavior is manifested in the temporal changes of the following Bragg spots: $(8k6)$ shown in Fig. 3d ($k = 0, \pm 1, \pm 2, \pm 3$ or ± 4); $(10\ 2\ 4)$, (915) , (806) , $(7\bar{1}\ 7)$, $(6\bar{2}\ 8)$, $(10\ 1\ 6)$, (907) , $(8\bar{1}\ 8)$, (923) , (814) , and $(5\bar{2}\ 7)$ in Fig. 3e; (606) , (714) and $(4\bar{1}\ 7)$ in Fig. 3f. In contrast, the slower picosecond behavior is not affected by the electron pulse width, and has a time constant (τ_2) of 9.2 ps (Fig. 6c). Such dynamics is observed for the (091) , (084) and $(08\bar{2})$ Bragg spots from the single crystal and also for the (040) from the thin-film sample.

We check the temporal changes of the background intensity in the vicinity of the (806) diffraction. Unlike 20% intensity decrease for the spot at $10.2\ \text{mJ}/\text{cm}^2$, the intensity of inelastic scattering exhibits essentially no dynamics and maintains a constant level, as shown in Fig. 7a. Therefore, the difference patterns presented in Fig. 5 do not originate from an overall decrease in the number of diffracted electrons that might be caused by the photoinduced insulator–metal transition. They reveal real structural changes during the transformation. The positions and widths of the intensity-decreasing Bragg spots have no significant dynamics at early times, as demonstrated in Fig. 7, panels b and c, respectively. For comparison, a clear Bragg spot movement as large as 2.5% (Ch. 7) and a distinct width broadening of more than 50% (Ch. 4) have been observed in different

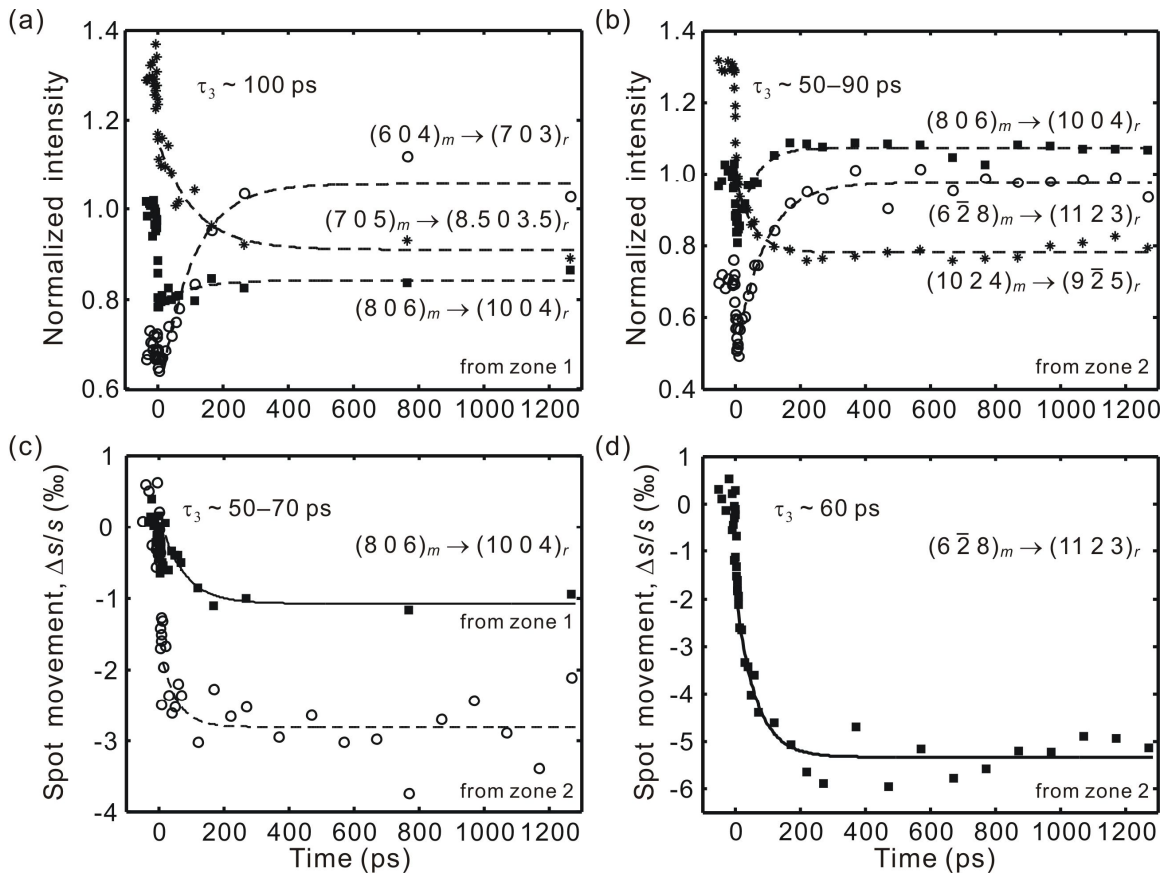


Fig. 8. Long-time change in (a and b) the diffraction intensities (offset vertically by a constant value for clarity) and (c and d) the positions, obtained from the experiments at different zone axes. Indices of the Bragg spots for the M_1 phase and their conversion into the high-temperature ones are provided. The temporal profiles are fitted to a single exponential decay function, and the extracted time constant (τ_3) is given in each panel. These values are similar and, therefore, indicate the time scale for the final lattice conversion from the M_1 phase to the high-temperature one. After the conversion is complete, the diffraction intensities and positions remain for >1 ns.

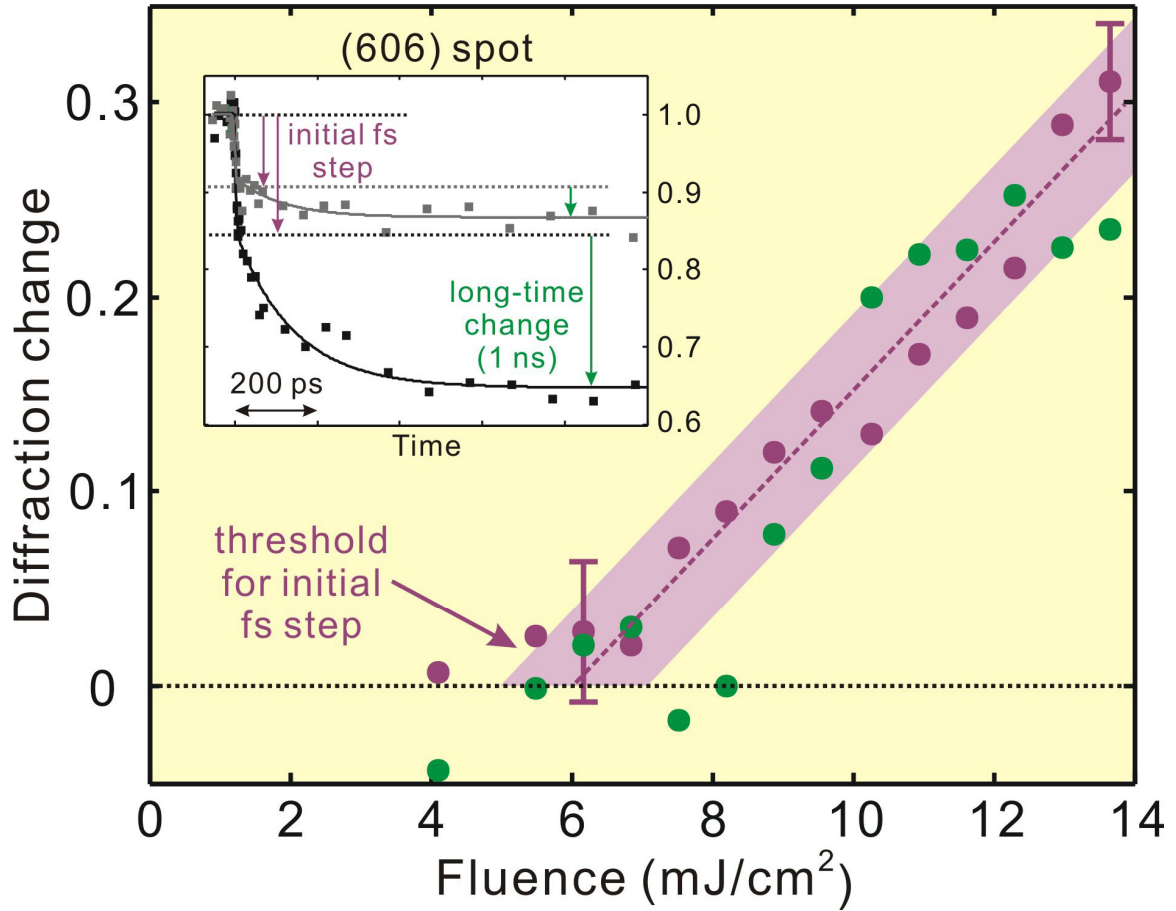


Fig. 9. Dependence of the femtosecond dynamics and the large-scale shear displacement on excitation fluence at room temperature. The magnitude of the initial intensity decrease (violet) and the amplitude of the long-time change (green) are plotted for different excitation fluences. A common threshold region is observed. The inset shows the transients of the (606) Bragg spot for two different excitation fluences. The magnitudes of change were measured at 10 ps and 1 ns.

materials. Thus, the particular manner of the diffraction changes presented here signifies a different transformation mechanism from those reported in other studies.

At a later time, the VO₂ structure has to complete its transition into the tetragonal form. The further changes in the Bragg spot intensities and positions within the experimental time range are shown in Fig. 8. The common feature in these transients is the evolution of diffraction change toward a final value with a time constant (τ_3) of 50~100 ps, followed by its maintenance for 1 ns or longer. Intensity increases and decreases for different spots are observed (Fig. 8, panels a and b), depending on the diffraction indices and also the overlap between the reciprocal lattice points and the Ewald sphere after the structural transformation; more discussion will be given in the next section. For the spot positions, as plotted in Fig. 8, panels c and d, as two examples, we observe ~0.1% (~0.3% in another measurement) and ~0.5% decrease in the reciprocal vectors of the (806)_m and (6 $\bar{2}$ 8)_m spots, respectively. The calculated changes for these two spots are -0.23~0.33% and -0.19~0.44%, depending on the unit-cell parameters used (15, 16); it is noted that these values may need some adjustments due to the slight tilt of the axes (31). However, according to the good agreement between our experimental observations and the calculations based on the static structures from x-ray diffraction, we conclude that completion of the transformation to the tetragonal structure occurs on a time scale of ~100 ps after the femtosecond photoexcitation.

After the identification of the short-term and long-term dynamics, fluence dependence of the diffraction intensity was studied at room temperature for two time points, $t = 30$ ps and $t = 1.3$ ns, as shown in Fig. 9 for the (606) Bragg spot as an example. The intensity change displays a nearly linear dependence with a threshold (F_{th}) at 6 ± 1 mJ/cm² (53). Given the reflectivity (R) of 0.28 and the optical penetration depth

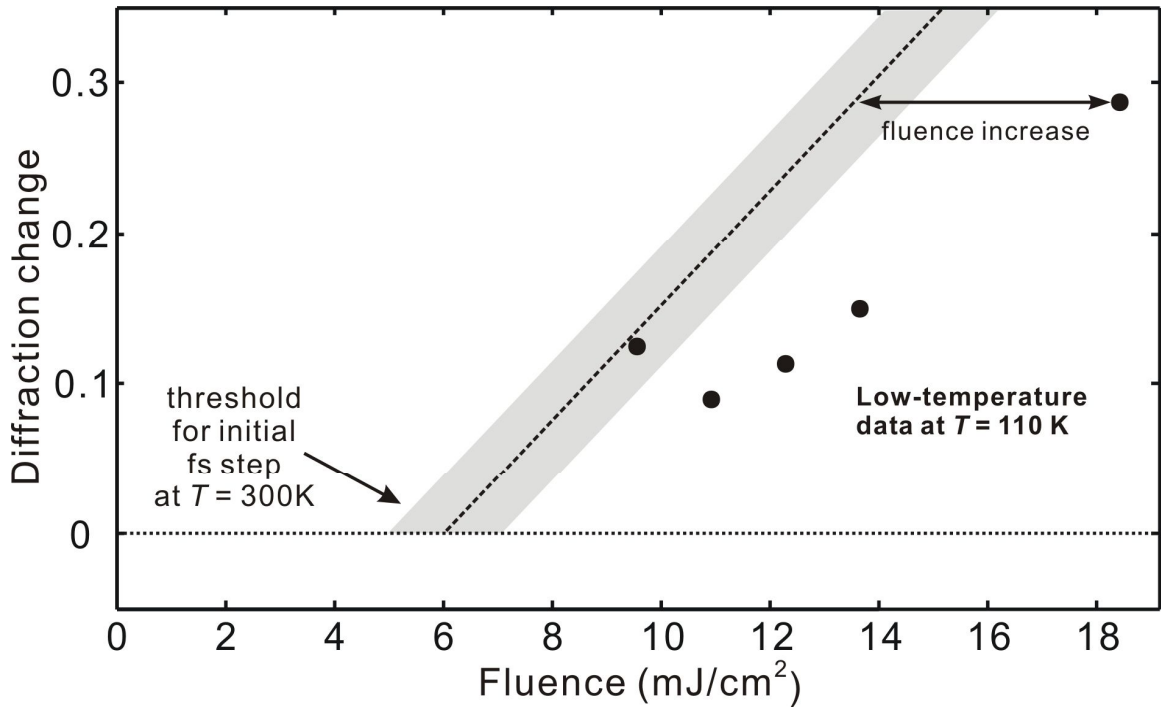


Fig. 10. Comparison of the fluence dependence of the femtosecond dynamics at two temperatures. The dashed line and the shaded region are the same as those in Fig. 9 for room temperature. At $T = 110$ K, an increased fluence (indicated by the horizontal arrow) is required for the observation of the same level of initial intensity decrease at $T = 300$ K.

($1/\alpha$) of ~ 100 nm at 800 nm (54), this threshold fluence corresponds to an optical density of $F_{\text{th}}(1-R)/(1/\alpha) = 430$ mJ/mm³ absorbed at the surface. With the unit cell volume of 118 \AA^3 (16), which contains four vanadium ions, such an energy density gives ~ 0.05 photon per vanadium ion, indicating the minimum fluence required for switching into the new phase in crystalline VO₂. For the spots that exhibit the femtosecond dynamics, the threshold for the sub-nanosecond component is either the same or slightly higher than that for the femtosecond component (Fig. 9), suggesting that the appearance of the long-time dynamics is associated with the initiation of the short-time dynamics.

Prompted by the coincidence between the threshold energy density of

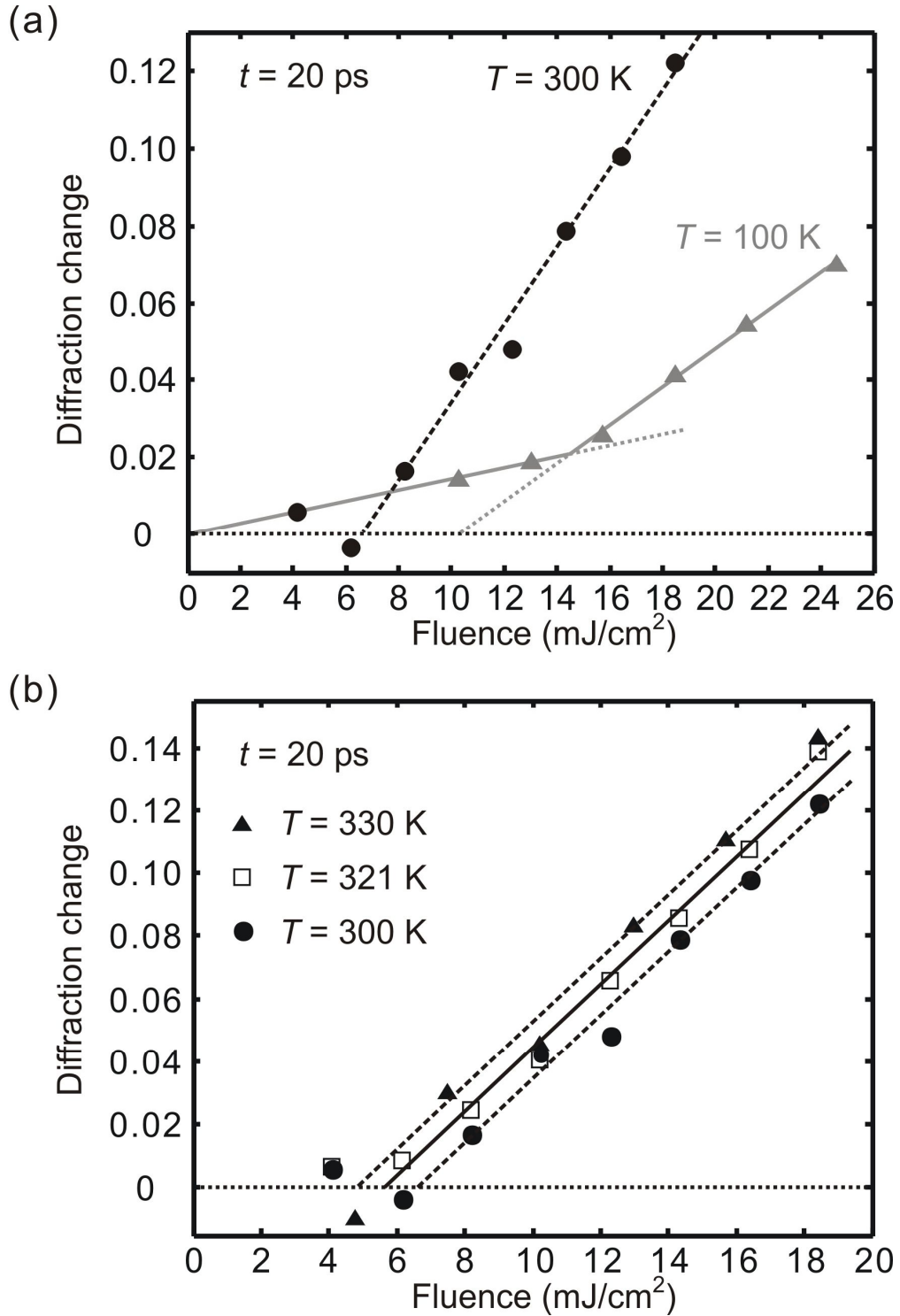


Fig. 11. Fluence dependence of the initial intensity decrease (measured at $t = 20$ ps) for different temperatures. The specimen is a VO_2 film (140 nm in thickness) deposited on $\text{Al}_2\text{O}_3(10\bar{1}0)$. The thin-film results agree well with those obtained from the VO_2 crystals.

$430 \pm 72 \text{ mJ/mm}^3$ (i.e., $\sim 1800 \pm 300 \text{ cal/mole}$) and the minimum thermal energy necessary for the phase transition from $T = 300 \text{ K}$ [i.e., the required enthalpy increase of $\sim 550 \text{ cal/mole}$ plus the latent heat of 1020 cal/mole (4)], we set off to investigate the influence of the temperature on F_{th} for the photoinduced transformation. The temporal evolution of diffraction changes at $T = 110 \text{ K}$ is found to be similar to the observation at room temperature. Intriguingly, much larger excitation fluence is required to cause an initial intensity decrease of 30%; the general trend obtained from the low-temperature experiment provides good evidence for an increased threshold (Fig. 10). To verify this observation, we also conducted similar experiments on a thin-film specimen, $\text{VO}_2/\text{Al}_2\text{O}_3(10\bar{1}0)$. The results, presented in Fig. 11a, show a satisfactory agreement: practically the same threshold of $F_{\text{th}} \sim 6 \text{ mJ/cm}^2$ is obtained at room temperature and a larger one for the low temperature. Moreover, this threshold fluence becomes lower at temperatures higher than 300 K but below 340 K (Fig. 11b). Such a coincidence between the photoexcitation threshold observed in the current dynamics study and the thermal energy mandated by thermodynamics may be the pivotal connection between the two approaches, dynamical and static, for the study of VO_2 . Its importance and implications are discussed in the next section.

Discussion

A. Short-time Dynamics: V–V Bond Dilation and Intracell Adjustment

The absence of a spot shift at early times signifies that no lattice expansion takes place on the ultrashort time scale as a result of the optical excitation (Fig. 7b). In addition, the absence of a clear width change indicates that no significant lattice disorder is introduced (Fig. 7c). Thus, structural modification on a larger scale across many unit cells

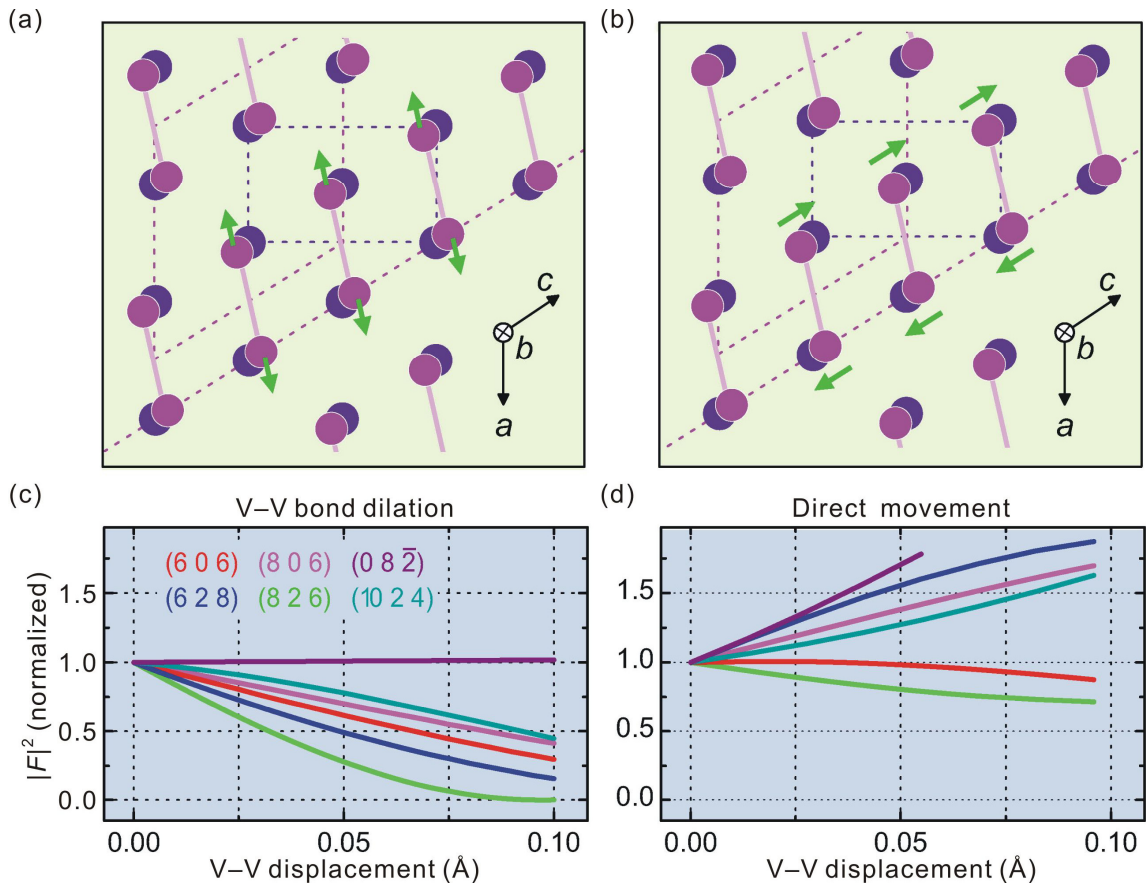


Fig. 12. Atomic movements and the calculated structure factors. (a) Indirect motion of the vanadium ions from the initial (purple) to the final (blue) positions, with the initial step being the displacement of the vanadium ions along the chemical bonds that are mostly along the monoclinic *a* axis. The monoclinic unit cell is depicted as dotted purple lines and the tetragonal unit cell as a blue dotted box. (b) Direct motion of the vanadium ions from the initial (purple) to the final (blue) positions, mostly along the monoclinic *c* axis. The indicated displacements in panels a and b are for delocalized excitation of the lattice. (c) Structure factor and expected intensity change for the listed Bragg spots for the displacement depicted in panel a. (d) Structure factor and intensity change for the displacement depicted in panel b.

is not significant during this time range. These observations also exclude thermal expansion or lattice inhomogeneity (strain) as an important mechanism to consider.

In contrast, the intensities of Bragg spots are influenced by the photoexcitation of valence electrons, signifying that additional atomic motions take place within the unit cell and cause destructive interference to diffraction. Notably, all Bragg spots that show the femtosecond behavior involve nonzero values for the h , k and l indices, whereas those displaying the slower picosecond behavior have a zero h index. This distinct difference confirms that the photoexcited material is in a highly nonequilibrium state, and the diffraction intensity decrease cannot be explained by the Debye–Waller factor (Eq. 16 of Ch. 2) derived on the basis of thermal equilibrium. Furthermore, the two behaviors with a clear difference in the time constants signify stepwise atomic motions along different directions. Thus, we should return to the structure factor and consider the possible atomic movements for the observed diffraction changes.

The intensity (I) of the Bragg spot (hkl) is proportional to the square of the structure factor, $F(hkl)$, which is determined by the position (xyz) of atom j within the unit cell,

$$F(hkl) = \sum_j f_j \exp[-2\pi i(hkl) \cdot (xyz)_j]; \quad I(hkl) \propto |F(hkl)|^2, \quad (1)$$

where f_j is the atomic scattering factor. The initial and final vanadium positions in the two phases are depicted in Fig. 12, panels a and b. From the inner product in Eq. 1, it is evident that an atomic movement along a certain direction can only affect those Bragg spots with nonzero components in the Miller indices along that direction. Thus, it is concluded from the experimental results that the initial femtosecond motion is mostly along the a axis, which also corresponds to the direction of the V–V bonds in the M_1 structure (Fig. 12a). On the other hand, the picosecond structural transformation projects

along the c and b axes. If the femtosecond motion had significant components along b or c , it should be manifested in the dynamics of all investigated spots, contrary to the observations. Note that the direct structural evolution from the initial M_1 to the final tetragonal phase is mostly along the c axis (Fig. 12b). Therefore, the argument in the Introduction Section is justified: the photoinduced phase transformation of VO_2 involves not only the initial and final states but also transitional structures which appear on the femtosecond and picosecond time scales. The observed stepwise atomic motions indicate that the phase transition proceeds through a nondirect pathway on the multidimensional potential energy surface, and not through a direct structural conversion.

To quantify the short-time structural changes, we calculate for the observed Bragg diffractions the structure factor and intensity changes as a function of the atomic displacement. In Fig. 12c, the results of the V–V bond-weakening (or dilation) motion is displayed. All spots with a nonzero h index show a decrease in intensity and for those with $h = 0$, the intensity remains nearly unchanged, as experimentally observed on the femtosecond time scale. In contrast, the direct transformation from the initial to the final structure would cause most spots to show an increase, and some a decrease, in the $|F|^2$ value (Fig. 12d), a behavior which disagrees with the observation within an ultrashort time. It is noted that in the limit of delocalized, uniform excitation across all excited unit cells, even a small-amplitude motion of V–V bond dilation on the order of 10^{-2} Å can cause a substantial decrease in diffraction intensity. This effect is likely to have its origin in the symmetry of the structure: the M_1 phase has a lower symmetry and the structural transformation is a symmetry-raising process.

The initial photoexcitation of the valence electrons in VO_2 may be more localized instead of being uniformly distributed. We also consider this localized scenario by

calculating the $|F|^2$ value with four random (instead of all 54) dilated bonds in a $3 \times 3 \times 3$ supercell. The results are very similar to those plotted in Fig. 12c, except for a larger V–V separation. For the same amount of intensity decrease, this localized scenario requests ~ 10 times the V–V displacement obtained from the delocalized scenario, which is on the order of 10^{-1} Å. Such an amount of displacement is a large fraction of the difference between the two V–V bond lengths in the M_1 phase (i.e., 0.588 Å), which can reasonably be the beginning step for the transformation to the equal V–V distances as in the tetragonal phase.

The femtosecond V–V bond dilation can be readily understood from a chemical perspective. The initiating excitation at 1.55 eV is primarily from the $d_{||}$ band that has major contribution from the bonding of vanadium pairs (5, 19) to an antibonding state that instantly results in a repulsive force on the atoms. Consequently, they separate along the bond direction in an ultrashort time faster than $\tau_1 = 307$ fs, which is already less than twice the V–V vibrational time of ~ 170 fs (28). In sequence and on a slower time scale, all atoms in the unit cell adjust themselves under the influence of the new electronic state, towards the configuration of the tetragonal phase. These two successive stages of structural evolution constitute the short-time dynamics.

It is worth noting that the dominance of the femtosecond dynamics emerges when the relevant direction of diffraction is monitored; the picosecond component originates from the transversal motion. Therefore, it is expected to see a composite transient behavior in optical reflectivity or diffraction experiments on polycrystalline samples because of the averaging over all orientations. A previous study using time-resolved x-ray diffraction (24) reported that the temporal evolution of intensity increase around the (011)-spot region (55) from a crystal is dominated by a 12-ps profile, with a relatively

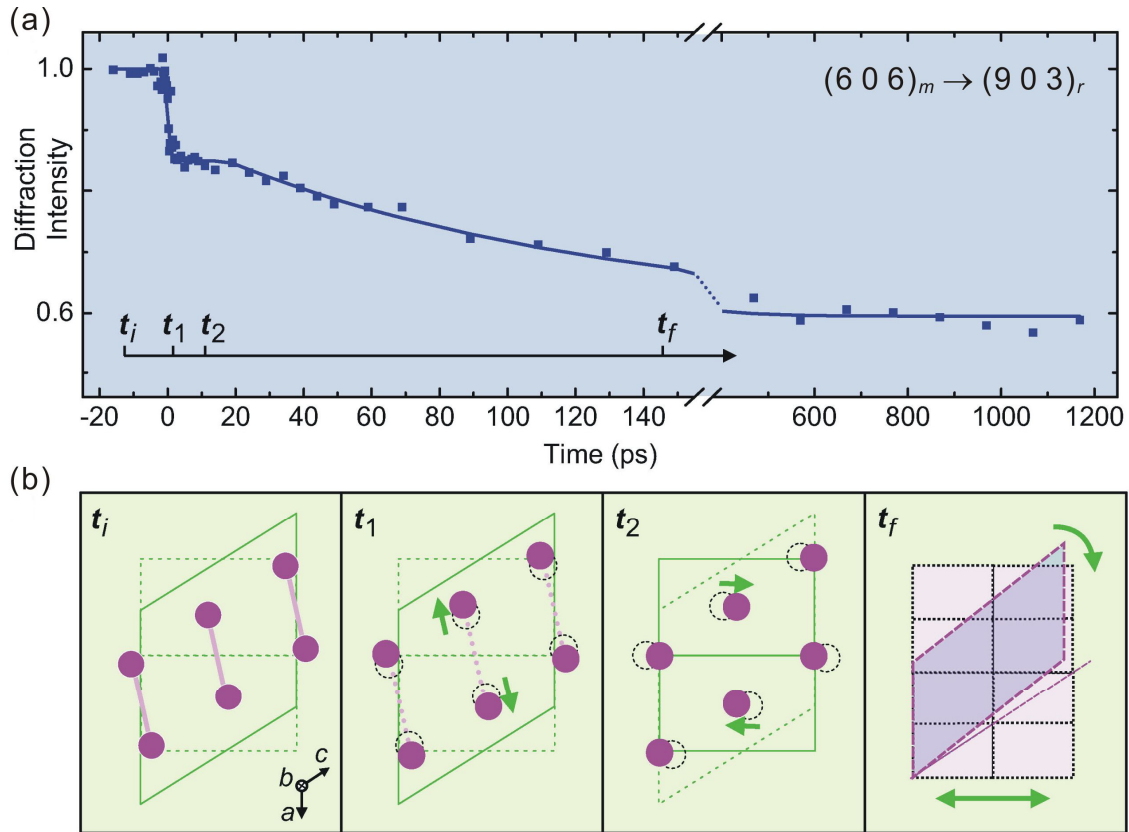


Fig. 13. Transitional structures during the ultrafast phase transformation. (a) The experimental data, here the $(606)_m$ -spot (blue), reflects the stepwise atomic motion within the unit cell and, on larger length scales, of shear motion. The important times during the transformation are indicated (t_i : before photoexcitation; t_1 : after the femtosecond process; t_2 : after the picosecond process; t_f : on a longer time scale). (b) Structural changes at the corresponding times (t_i , t_1 , t_2 , t_f).

small faster component (≤ 500 fs). In this work, the transitional structures *en route* to the stable tetragonal configuration are resolved, and distinct coordinates can be defined for the energy landscape of the current photoinduced phase transformation. The overall temporal behavior, up to 1.2 ns, and structural snapshots are presented in Fig. 13 (see below for the long-time dynamics).

Before our recent report on direct probing of the photoinduced structural transformation in VO₂ (46), Cavalleri *et al.* reported the ultrafast optical reflectivity changes with a bottleneck time scale believed to be limited by the structure and related to the stretching and tilting of V–V dimers (28). Lately, Kübler *et al.* reported coherent structural dynamics of polycrystalline VO₂ within the first picosecond using multi-THz conductivity (27). From the spectral region related to the IR-active phonon resonances, they observed oscillations centered at 6 THz and provided a qualitative model with the initial dynamics being the local excitation of molecular V–V dimers into an antibonding state. Here, we want to point out that, while the same initial femtosecond mechanism is reported, this is the first time that the transitional structures are directly resolved and the whole transformation process is mapped up to a nanosecond time. The current study on VO₂ well demonstrates the capability of UEC.

The comparison of $\tau_1 = 307$ fs (an upper bound) with the 80-fs time constant from optical reflectivity (28) or with the ≤ 500 -fs one from X-ray diffraction (24) is not straightforward, as the former approach is more sensitive to the changes in the electronic configuration of the material whereas the latter integrates the structural changes over the X-ray probing length of micrometers. Future experiments with a ≤ 100 -fs temporal resolution may unravel the time scale of the femtosecond dynamics to be half of the vibrational time (~ 170 fs) of the equilibrium structure, or one or two vibrational periods due to potential-driven motion (Chs. 4 and 5) in the excited state (27). However, it is promising to infer the answer based on the observed threshold behavior (see below).

B. Long-time Dynamics: Carrier Diffusion and Lattice Shear Motion

The transient behavior on the longer, sub-nanosecond time scale reveals another dimension of the structural dynamics. As shown in Fig. 8, after the initial insulator–metal

transition, there is a continuous temporal change in the spot intensities and positions which levels off at $t \sim 300$ ps. Specifically, the movements of the $(806)_m$ and $(6\bar{2}8)_m$ Bragg spots toward their corresponding positions predicted by the tetragonal structure do not start immediately after the femtosecond optical excitation (Fig. 7b), but proceed after the short-time (femtosecond and picosecond) structural dynamics (Fig. 8, panels c and d). The observation leads us to the conclusion that, within the photoexcited region, the final tetragonal structure is not fully achieved until few hundred picoseconds. The optical reflectivity experiment showed that a metallic state is already reached and maintained after the femtosecond dynamics (28). Therefore, the resolved transitional states during the picosecond dynamics (Fig. 13b, t_1 to t_2) and the sub-nanosecond evolution (Fig. 13b, t_2 to t_f) can be assigned as metallic monoclinic and unexpanded metallic tetragonal states, respectively. The existence of a metallic intermediate state with a monoclinic geometry (21) is also confirmed, although it is ultrashort-lived in nature (56).

With the time scale of ~ 100 ps in mind, we first examine the possibility of thermal diffusion as the dominant mechanism. The thermal diffusivity coefficient (κ) of VO₂ at $T = 300$ K is $0.021 \text{ cm}^2/\text{s}$, calculated from the relation $\kappa = K/\rho C_l$ where $\rho = 4.67 \text{ g/cm}^3$ is the density, $C_l = 0.67 \text{ J/(g}\cdot\text{K)}$ is the specific heat and $K = 0.066 \text{ W/(cm}\cdot\text{K)}$ is the thermal conductivity (4). From the optical penetration depth of ~ 100 nm and the equation of thermal diffusion in one dimension,

$$\frac{\partial T}{\partial t} = \kappa \frac{\partial^2 T}{\partial z^2},$$

we calculate that major heat conduction away from the probed layer must be slower than 1 ns (57). In fact, a simple estimation of the characteristic time for the absorbed heat to be well removed from the 100-nm excited region is $(100 \text{ nm})^2/4\kappa \sim 1.2$ ns. Thus, thermal

diffusion itself cannot explain the observed ~ 100 -ps dynamics, and is likely a minor factor to consider.

Carrier diffusion within the excited, metallic region, on the other hand, may have a time constant that is on the correct order of magnitude. The carrier diffusion coefficient D_c may be estimated with the use of the Einstein relation, $D_c = \mu \cdot \frac{k_B T}{q}$, where μ is the carrier mobility in the metallic phase, k_B is the Boltzmann constant and q is the charge of a carrier. If q is assumed to be the unit charge and μ is on the order of $1\text{--}10 \text{ cm}^2/(\text{V}\cdot\text{s})$ (4), D_c will be on the order of $0.1 \text{ cm}^2/\text{s}$, resulting in a diffusion curve resembling to an exponential decay with a time constant of ~ 100 ps and, therefore, matching with the observation. The relevance of carrier diffusion in the structural dynamics is the following. Excess electrons (carriers), which are not bound by strong correlation with the lattice, may redistribute within the excited metallic region but are impeded by the insulating surrounding. The diffusion of carriers from the surface region of higher carrier density to the less dense bulk means a partial removal of excitation from the electron-probed region, leaving a partial transformation behind. This may explain why the $(705)_m$ spot in Fig. 8a, which is forbidden in the tetragonal structure, does not fully disappear at an intermediate fluence; its intensity does go to zero when a higher fluence is applied (data not shown).

In addition to carrier diffusion, another crucial (maybe even more important) mechanism is the motion of shear and expansion/contraction (Fig. 13b, t_f). The diffusion of electrons into the deeper region may contribute to the generation of this motion, too. As mentioned in the Introduction Section, shear is inevitable for the macroscopic formation of the tetragonal phase. From the static x-ray diffraction measurements, the small angular movements of nearly all Bragg spots upon the phase transition (Fig. 2b)

indicate a slight rotation of the crystallographic axes (31), which is equivalent to a shear motion. As it travels at the sound speed of ~ 4000 m/s in VO₂ for a length scale of few hundred nanometers, the time scale is also tens of picoseconds and corresponds well with the observation. This shear motion is further supported by the evolution of Bragg spot intensities. Although the Bragg spots exhibit the same early femtosecond-to-picosecond behavior, they show intensity increase or decrease at the sub-nanosecond scale for different zone axes. Because not all Bragg spots equally well coincide with the Ewald sphere at the same time, shear motion may enhance or suppress the Bragg intensities besides the changes given by the structural transformation. The asymmetric change shown in Fig. 5b is a good example.

We have given a full account of the photoinduced structural dynamics at short and long times, and also distinguished the different stages and the mechanisms involved during the phase transformation. Because of the similar dynamics observed at different fluences, we are able to compare the extent of the diffraction change from a fluence-dependent study at two characteristic times. A different sample temperature does not affect the dynamical behaviors, thus the direct comparison of thresholds retrieved at different temperatures is also feasible.

C. Threshold Behavior: Dynamics vs Thermodynamics

The existence of an excitation threshold for the initiation of the femtosecond V–V bond dilation shows that, from a delocalized energy-band perspective, a minimum density of photodoping is necessary for the change of the band structure into a metallic configuration together with the structural modification. From a chemical perspective, a minimum level of charge excitation (i.e., enough bond weakening) is needed to cause an irrecoverable motion. The requirement of ~ 0.05 photon per vanadium (equivalent to one

electron for every 20 V^{4+} ions) at room temperature is quite low as compared to an electron provided by each V^{4+} ion (its electronic configuration is $3d^1$). This result gives some hints about the easiness of perturbing the VO_2 system. Below this threshold the V–V bond is simply set on a coherent vibrational motion (27, 28), although its bond strength is slightly reduced.

Intriguingly, a diffraction intensity decrease due to the induced additional motion of V–V vibration is not clearly discernible when the excitation fluence is below the threshold (Fig. 9). Here is a puzzling inconsistency: according to the scenario of delocalized excitation in Fig. 12c, an intensity decrease would always be present and no threshold behavior would be expected, because the atomic movement for the V–V displacement (on the order of 10^{-2} Å) is comparable to a typical increase in the vibrational amplitude. This puzzle may be resolved by adopting the scenario of localized excitation. At an optical fluence lower than the threshold, because the dispersed excited units cannot form the required connectivity for the macroscopic structural transformation, the strongly correlated material VO_2 only allows an additional vibrational amplitude (on the order of 10^{-2} Å) to be added to the existing V–V thermal motion at room temperature. As mentioned previously, an appreciable decrease in the Bragg spot intensity in this picture needs a V–V displacement (not simply vibration) on the order of 10^{-1} Å. Therefore, it is consistent to observe no appreciable intensity decrease at low fluences. Above the threshold, V–V bond dilation initially occurs at various localized places, with a density higher than one pair per 20 vanadium sites (i.e., per 5 unit cells) to ensure the connectivity through strong correlation; immediately following this initial excitation, the equilibration and intracell adjustment take place in all adjacent unit cells on the picosecond time scale, signifying a collective motion. This mechanism may be regarded

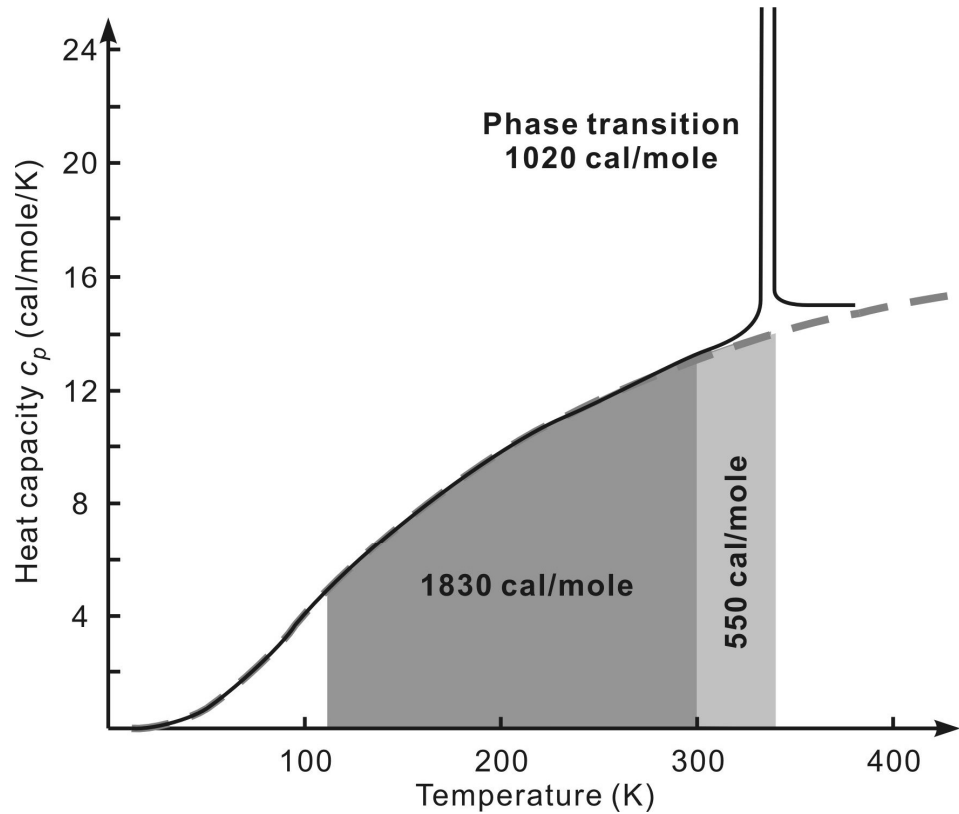


Fig. 14. Heat capacity of VO_2 as a function of temperature (solid lines). The dashed line is the theoretical value for Debye temperature of 750 K (4). The values given in the shaded regions are the enthalpy increase required for the corresponding temperature rise. The latent heat for the phase transition equals to 1020 cal/mole.

as the dynamical version of the percolation model considered in temperature-dependent studies (10, 58).

The fact that the threshold for the sub-nanosecond component is not below that for the femtosecond component (Fig. 9) indicates the appearance of the long-time dynamics to be associated with the initiation of the short-time dynamics. The major implication is, regardless of the temperature of the material, the necessity of the initial femtosecond V–V bond dilation for the proceeding of the following dynamics, including the intracell adjustment, diffusion of nonbound carriers, lattice expansion/contraction and

shear motion. In other words, without the V–V bond dilation, VO₂ maintains the structural intactness in the M_1 phase.

It seems a pure coincidence for the optical density threshold at $T = 300$ K to be close to the minimum thermal energy mandated by the phase transition from the same temperature, if one considers the nature of the femtosecond localized excitation versus the overall macroscopic change in the energy content through thermal means. However, the influence of temperature on the observed threshold strengthens this correlation. If correct, according to Fig. 14, a fluence threshold of 11.3 mJ/cm^2 at $T = 110$ K (or equivalently, an increase of $\sim 6 \text{ mJ/cm}^2$ relative to the room-temperature value, 5.2 mJ/cm^2 derived from the thermodynamic value) is expected; at a temperature just below the transition, a threshold of 3.4 mJ/cm^2 (or a decrease of 1.8 mJ/cm^2) is anticipated. Experimentally, the shift by $\sim 4.5 \text{ mJ/cm}^2$ in Fig. 10 for observing a similar degree of diffraction change at 110 K, and the threshold increase of $4\text{--}8 \text{ mJ/cm}^2$ at 100 K in Fig. 11a, give a fairly good agreement with the expected increase of 6 mJ/cm^2 . The observed threshold decrease of $\sim 2 \text{ mJ/cm}^2$ at $T = 330$ K in Fig. 11b also makes a good match. Thus, the strong correlation between the optical and thermal energy values at various temperatures encourages a serious comparison between the dynamical behavior of VO₂ and its thermodynamic properties.

In fact, there are other studies reporting a similar fluence threshold at room temperature and some mentioning the trend for the temperature dependence. From a VO₂ film, a threshold of 3 mJ/cm^2 was measured by femtosecond infrared absorption (26). From a polycrystalline thin film, the thresholds observed by multi-THz conductivity were 5.3 , 4.6 and 3 mJ/cm^2 at $T = 250$, 295 and 325 K, respectively (27). From an oriented thin film, the extrapolated threshold from the photoinduced conductivity measurements

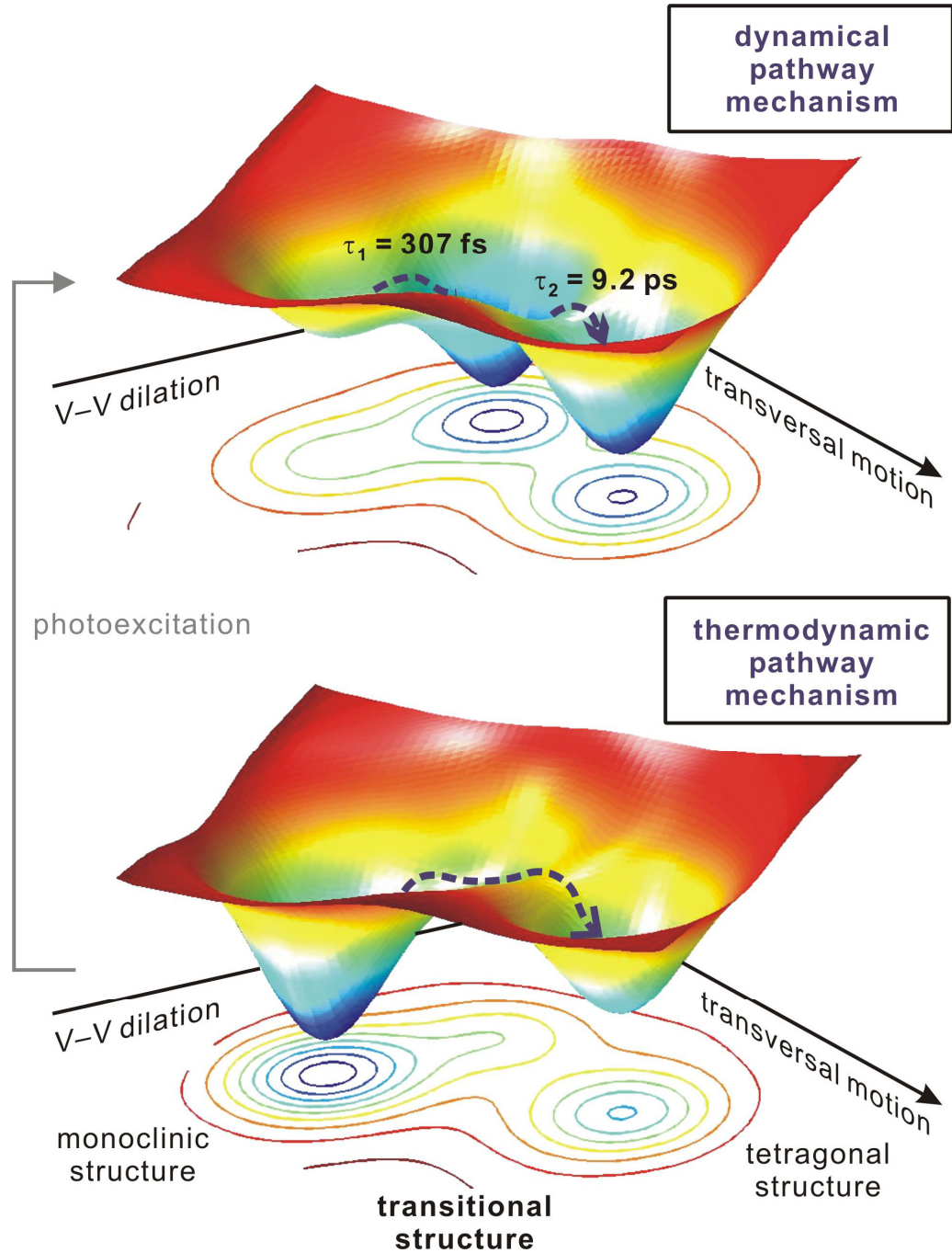


Fig. 15. The stepwise mechanism for the insulator–metal, monoclinic–tetragonal phase transition of VO_2 , through the photoexcitation (upper panel) or the thermal means (lower panel). Structural intermediates are involved in the transformation process, and the initial step is the dilation of V–V dimers in the M_1 phase. A change in temperature leads to the change in the relative energies of all three (initial, intermediate and final) states.

decreased from 7 mJ/cm^2 at $T = 300 \text{ K}$ to 2 mJ/cm^2 at 330 K (58). The general agreement for the threshold value from various groups and different samples, and its temperature dependence following a similar trend, further support the aforementioned correlation.

The common theme shared by the VO_2 structural dynamics and several recent studies on the static electronic structure (12, 13, 19) is the crucial role of the V–V dimer unit. On the basis of this understanding and the correlation between the optical and thermal energy thresholds, we propose a common transformation mechanism: the phase transition from the insulator (M_1) to metal (tetragonal) state is initiated by the dilation of the correlated/connected V–V bonds, whether it is induced optically or thermally. An illustration is given in Fig. 15: the relative energies of the initial, transitional intermediate and final states will be affected by temperature which may facilitate or hinder the transformation. In a static picture, the band gap of $\sim 0.6 \text{ eV}$ for the M_1 phase (4, 13), which is more than 20 times the thermal energy of 29.3 meV at 340 K , cannot be theoretically reproduced without a simultaneous consideration of the structural aspect and correlation within singlet V–V pairs (19). The molecular, correlated nature of V–V dimers in the M_1 phase cannot be fully described either by the Mott-Hubbard (electron correlation) model or by the Peierls dimerization (12). Treating a V–V pair as one molecular unit, which is also supported by the current results of structural dynamics, becomes the key to understanding the thermodynamic and dynamical properties of VO_2 .

Since the structural and electron correlation effects are intertwined, the allegation of different temperatures for the insulator–metal and structural phase transitions may become poorly supported (21, 56). However, transitional intermediates do exist on an ultrashort time scale, as shown in this work. In regard to the femtosecond V–V bond dilation, considering the molecular and correlated nature of the dimers, one may expect

the time constant, τ_1 , to be roughly half of the vibrational time of 170 fs if an inertial separation is operative, which matches with the optical reflectivity results (28); or about one vibrational cycle if excitation is equilibrated and shared by several dimers, leaving the bond stretching motion to be in charge (27). According to our previous discussion about the scenario of localized excitation, we predict that the former mechanism is likely to occur with a much higher excitation fluence, whereas the latter is more probable for a fluence that does not exceed the threshold too much.

Conclusion

The advantage of using UEC to unravel the atomic motions during a structural phase transition is demonstrated by the results reported here for VO₂. The elementary steps follow a nonconcerted mechanism involving a sequence of transitional structures, first intracell atomic displacements on the femtosecond and picosecond time scales, followed by carrier diffusion and long-range shear motion within a sub-nanosecond time and at the speed of sound. The V–V bond dilation is the initial step of the insulator–metal transition and structural transformation, providing a dynamical molecular picture. The correlation between the thermal and photoinduced transition thresholds at different temperatures suggests the common pathway mechanism for the transition and connects the dynamics and thermodynamics research approaches into a unified description for this material. With four-dimensional atomic-scale spatial and temporal resolution, we expect, by using this table-top approach, many future extensions in the studies of strongly correlated materials and phase transformations, designed nanometer-scale materials and biological systems.

References and Footnotes:

1. P. Papon, J. Leblond, P. H. E. Meijer, *The physics of phase transitions: Concepts and applications* (Springer, New York, 2nd ed., 2006).
2. M. Imada, A. Fujimori, Y. Tokura, *Rev. Mod. Phys.* **70**, 1039 (1998).
3. P. P. Edwards, R. L. Johnston, C. N. R. Rao, D. P. Tunstall, F. Hensel, *Phil. Trans. R. Soc. A* **356**, 5 (1998).
4. C. N. Berglund, H. J. Guggenheim, *Phys. Rev.* **185**, 1022 (1969).
5. J. B. Goodenough, *J. Solid State Chem.* **3**, 490 (1971).
6. M. Marezio, B. McWhan, P. D. Dernier, J. P. Remeika, *Phys. Rev. B* **5**, 2541 (1972).
7. A. Zylbersztein, N. F. Mott, *Phys. Rev. B* **11**, 4383 (1975).
8. D. Paquet, P. Leroux-Hugon, *Phys. Rev. B* **22**, 5284 (1980).
9. S. Shin *et al.*, *Phys. Rev. B* **41**, 4993 (1990).
10. H. S. Choi, J. S. Ahn, J. H. Jung, T. W. Noh, D. H. Kim, *Phys. Rev. B* **54**, 4621 (1996).
11. K. Okazaki *et al.*, *Phys. Rev. B* **69**, 165104 (2004).
12. M. W. Haverkort *et al.*, *Phys. Rev. Lett.* **95**, 196404 (2005).
13. T. C. Koethe *et al.*, *Phys. Rev. Lett.* **97**, 116402 (2006).
14. F. J. Morin, *Phys. Rev. Lett.* **3**, 34 (1959).
15. G. Andersson, *Acta Chem. Scand.* **10**, 623 (1956).
16. K. D. Rogers, *Powder Diffr.* **8**, 240 (1993).
17. T. M. Rice, H. Launois, J. P. Pouget, *Phys. Rev. Lett.* **73**, 3042 (1994).
18. R. M. Wentzcovitch, W. W. Schulz, P. B. Allen, *Phys. Rev. Lett.* **72**, 3389 (1994).

19. S. Biermann, A. Poteryaev, A. I. Lichtenstein, A. Georges, *Phys. Rev. Lett.* **94**, 026404 (2005).
20. M. M. Qazilbash *et al.*, *Science* **318**, 1750 (2007).
21. H.-T. Kim *et al.*, *Phys. Rev. Lett.* **97**, 266401 (2006).
22. M. F. Becker *et al.*, *Appl. Phys. Lett.* **65**, 1507 (1994).
23. M. F. Becker *et al.*, *J. Appl. Phys.* **79**, 2404 (1996).
24. A. Cavalleri *et al.*, *Phys. Rev. Lett.* **87**, 237401 (2001).
25. G. I. Petrov, V. V. Yakovlev, J. A. Squier, *Opt. Lett.* **27**, 655 (2002).
26. A. Cavalleri *et al.*, *Phys. Rev. Lett.* **95**, 067405 (2005).
27. C. Kübler *et al.*, *Phys. Rev. Lett.* **99**, 116401 (2007).
28. A. Cavalleri, T. Dekorsy, H. H. W. Chong, J. C. Kieffer, R. W. Schoenlein, *Phys. Rev. B* **70**, 161102(R) (2004).
29. K. Sokolowski-Tinten *et al.*, *Nature* **422**, 287 (2003).
30. D. Maurer, A. Leue, R. Heichele, V. Müller, *Phys. Rev. B* **60**, 13249 (1999).
31. D. Kucharczyk, T. Niklewski, *J. Appl. Cryst.* **12**, 370 (1979).
32. K. J. Caspersen, E. A. Carter, *Proc. Natl. Acad. Sci. USA* **102**, 6738 (2005).
33. D. R. Trinkle *et al.*, *Phys. Rev. Lett.* **91**, 025701 (2003).
34. C. Bressler, M. Chergui, *Chem. Rev.* **104**, 1781 (2004).
35. A. Rousse, C. Rischel, J. C. Gauthier, *Rev. Mod. Phys.* **73**, 17 (2001).
36. K. Sokolowski-Tinten, D. von der Linde, *J. Phys.: Condens. Matter* **16**, R1517 (2004).
37. M. Bargheer, N. Zhavoronkov, M. Woerner, T. Elsaesser, *Chemphyschem* **7**, 783 (2006).
38. K. J. Gaffney, H. N. Chapman, *Science* **316**, 1444 (2007).

39. H. E. Elsayed-Ali, G. A. Mourou, *Appl. Phys. Lett.* **52**, 103 (1988).
40. B. J. Siwick, J. R. Dwyer, R. E. Jordan, R. J. D. Miller, *Science* **302**, 1382 (2003).
41. H. Park, S. Nie, X. Wang, R. Clinite, J. Cao, *J. Phys. Chem. B* **109**, 13854 (2005).
42. A. H. Zewail, *Annu. Rev. Phys. Chem.* **57**, 65 (2006).
43. N. Gedik, D.-S. Yang, G. Logvenov, I. Bozovic, A. H. Zewail, *Science* **316**, 425 (2007).
44. M. S. Grinolds, V. A. Lobastov, J. Weissenrieder, A. H. Zewail, *Proc. Natl. Acad. Sci. USA* **103**, 18427 (2006).
45. V. A. Lobastov, J. Weissenrieder, J. Tang, A. H. Zewail, *Nano Lett.* **7**, 2552 (2007).
46. P. Baum, D. S. Yang, A. H. Zewail, *Science* **318**, 788 (2007).
47. W. Bruckner *et al.*, *Vanadiumoxide* (Akademie-Verlag, Berlin, 1983).
48. M. Borek, F. Qian, V. Nagabushnam, R. K. Singh, *Appl. Phys. Lett.* **63**, 3288 (1993).
49. D. H. Kim, H. S. Kwok, *Appl. Phys. Lett.* **65**, 3188 (1994).
50. Z. P. Wu *et al.*, *J. Phys.: Condens. Matter* **10**, L765 (1998).
51. S. Lysenko, V. Vikhnin, F. Fernandez, A. Rua, H. Liu, *Phys. Rev. B* **75**, 075109 (2007).
52. V. A. Lobastov *et al.*, in *Ultrafast Optics IV*, F. Krausz, G. Korn, P. Corkum, I. A. Walmsley, Eds. (Springer, New York, 2004), vol. 95, pp. 419-435.
53. The error bar is derived from the uncertainties in the experimentally observed intensity decreases, which were obtained by fitting the spot profiles. Depending on the approximation used for estimation of the fluence, e.g., whether an average value across a larger region or the peak value at center is calculated, an overestimation of $\sim 2 \text{ mJ/cm}^2$ may be present.

54. H. W. Verleur, A. S. Barker Jr., C. N. Berglund, *Phys. Rev.* **172**, 788 (1968).
55. Given the X-ray wavelength (1.54 Å) and diffraction angle (13.9°) reported (24), the Bragg peak should be indexed as (011) of the M_1 phase but was assigned as (110) of the M_1 phase (24). Upon transformation the peak becomes (110) of the tetragonal phase.
56. According to the reported X-ray diffraction patterns (21), the VO₂ phase involved was likely the M_2 phase (59) or a mixture of several structures, because the diffraction peaks that show temperature-dependent change do not correspond to the M_1 structure but can be related to the M_2 structure.
57. J. H. Bechtel, *J. Appl. Phys.* **46**, 1585 (1975).
58. D. J. Hilton *et al.*, *Phys. Rev. Lett.* **99**, 226401 (2007).
59. M. Marezio, B. McWhan, P. D. Dernier, J. P. Remeika, *Phys. Rev. B* **5**, 2541 (1972).